Earth, Planets and Space

FULL PAPER Open Access

Hydrogeological structure of a seafloor hydrothermal system deduced from a pair of positive and negative self-potential anomalies observed at the Oomuro-dashi hydrothermal field in the Izu-Ogasawara Arc, south of Japan

Yoshifumi Kawada[1,2*] and Takafumi Kasaya[1]

Abstract

This paper presents and interprets two new self-potential data measured over a hydrothermally active field associated with a Quaternary rhyolitic volcano, Oomuro-dashi, in the northern Izu-Ogasawara Arc, south of Japan. The measured data show a pair of positive and negative anomalies of the order of one millivolt at 5 m above the seafloor. The observation of a positive self-potential near a seafloor hydrothermal system is new, in spite that negative self-potential anomalies have been regularly reported in various studies for different locations. Determining the dominant mechanism(s) is therefore key to further understanding the subseafloor structure of seafloor hydrothermal systems. To this end, we also conducted long-term observations of subseafloor temperatures at two sites in the area of the self-potential anomaly to estimate the Darcy velocity. We found a downward fluid flow of the order of tens of metres per year at both sites. The flow in the area of the negative self-potential anomaly is stronger than in the area of the positive anomaly. Based on these observations, we propose two end-member models to explain the paired self-potential anomaly. The first model considers a horizontal geo-battery, in which part of a subhorizontal electrically conductive body is crossed by a subvertical redox front. In this model, the oxidised part of the geo-battery causes a negative self-potential anomaly, as in the previous observations, while the reduced counterpart of the geo-battery, which is normally buried, is exposed near the seafloor and causes a positive anomaly. In this case, a conductive body is expected to lie beneath both anomalies, and we could access the reduced part of the geo-battery. This model is consistent with the results of the Darcy velocity estimation if the strong hydrothermal circulation would cause the redox horizon to deepen. The second model is a combination of the thermal and streaming potentials causing both positive and negative self-potential anomalies. This model does not necessarily require a buried conductive body beneath the self-potential anomalies. These end-member models could be distinguished by resistivity imaging, which identifies the distribution of conductive bodies beneath self-potential anomalies, although they would overlap in natural systems.

Keywords Marine self-potential, Seafloor hydrothermal system, Volcanic activity, Geophysical exploration, Long-term temperature measurements, Electrochemical modelling, Thermal potential, Streaming potential

*Correspondence:
Yoshifumi Kawada
ykawada@g.ecc.u-tokyo.ac.jp
Full list of author information is available at the end of the article

Graphical Abstract

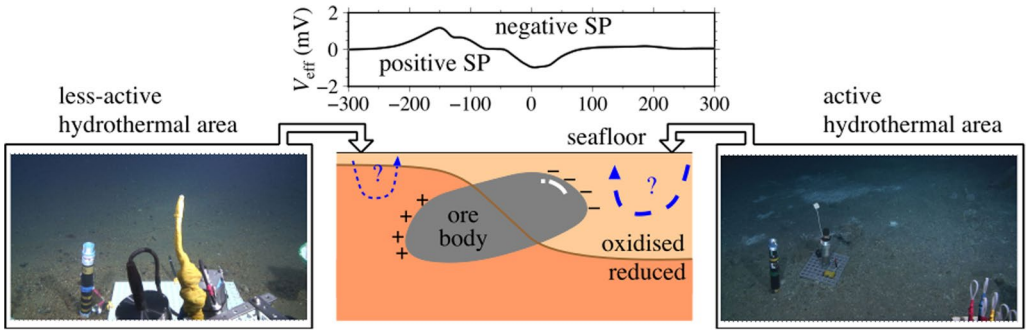

1 Introduction

The hydrogeological structure of seafloor hydrothermal systems plays an important role in the harvesting of microbial communities and the formation of hydrothermal precipitates (see, for example, the articles cited in Ishibashi et al. 2015). These properties can be attributed to both fluid flow patterns and crustal structures beneath the seafloor, and their detection is highly desirable. To this end, field measurements of crustal heat flow (Kinoshita et al. 2006; Masaki et al. 2011) and direct sampling of discharged hydrothermal fluids (Kawagucci et al. 2011; Ishibashi et al. 2014) and rock samples (Yoshizumi et al. 2015) have been carried out. However, these are collections of point-wise information with a local spatial scale such as a hydrothermal vent. On a larger scale of hydrothermal fields, such as kilometres, geophysical prospecting methods including seismic (Tsuji et al. 2012), geomagnetic (Honsho et al. 2016a, 2016b), and gravity (Evans 1996) surveys have helped to delineate hydrogeological structures beneath seafloor hydrothermal systems. Nevertheless, there is still a gap to be filled at these distant spatial scales to understand the subseafloor fluid flow structure.

The self-potential method has the potential to bridge the gap between the understanding of local or vent-scale properties revealed by in situ measurements and direct sampling, and the understanding of a field-scale structure imaged by geophysical prospecting. The self-potential is a naturally occurring electric potential (e.g. Zlotnicki and Nishida 2003; Jouniaux and Ishido 2012; Revil and Jardani 2013; Mehanee 2015) that responds to various processes involving charge transport (Nourbehechet 1963). The most important factors of interest include the redox potential, which responds to oxidation–reduction reactions (Sato and Mooney 1960), the streaming potential, which responds to fluid flow in the pore space via electrokinetic phenomena (e.g. Ishido and Mizutani 1981), and the thermal potential, in which temperature differences act as an electromotive force (e.g. Revil et al. 2013). Both streaming and redox potentials are involved in on-land environments, and self-potential measurements can image subsurface fluid flow (e.g. Jouniaux and Ishido 2012; Revil and Jardani 2013) and highly reduced contaminant plumes (e.g. Naudet et al. 2004). In contrast, in marine environments, the redox potential may be superior to the streaming potential due to weak electrokinetic phenomena caused by highly conductive pore fluids or seawater (Glover et al. 2012). The thermal potential is thought to be associated with magma bodies (Corwin and Hoover 1979) and underground coal fires (Revil et al. 2013), but theoretical investigations are under development. There is no application of the thermal potential to seafloor hydrothermal systems. In any case, it is expected that some hydrogeological information can be extracted from the self-potential signals.

To date, examples of self-potential anomalies above seafloor hydrothermal systems and ore deposits are mostly negative (e.g. Heinson et al. 1999, 2005; Sato et al. 2017; Safipour et al. 2017; Kawada and Kasaya 2017, 2018; Constable et al. 2018; Zhu et al. 2020; Su et al. 2022). These negative self-potential anomalies in marine environments can be understood by the redox-potential-driven geo-battery mechanism, which was originally proposed as a model to explain negative self-potential anomalies above mineral deposits on land (Sato and Mooney 1960). In the presence of a subsurface redox gradient with an oxidised (or high Eh) part near the seafloor and a reduced (or low Eh) part at depth, redox reactions around electrically conductive bodies such as sulphides will transport electrons upwards within these bodies, resulting in a negative self-potential anomaly above them. The observed negative self-potentials in marine environments may correspond to the oxidised part of the geo-battery of a vertically elongated conductive body crossing a horizontal

redox front. Note that in on-land environments, negative and positive self-potential anomalies have been observed separately or simultaneously at a single site (e.g. Corwin and Hoover 1979; Ishido 1981; Zlotnicki and Nishida 2003; Revil et al. 2023; Mehanee et al. 2023), probably due to a combination of different effects described above.

Here we report a pair of positive and negative self-potential anomalies detected by two deep-tow surveys conducted at the Oomuro-dashi hydrothermal field on the caldera floor of a Quaternary rhyolitic volcano in the northern Izu-Ogasawara Arc, south of Japan (Fig. 1), and propose new models to explain the observed paired self-potential anomaly. We also analyse the results of long-term observations of subseafloor temperatures, which are affected by variations in the bottom-water temperature due to the shallow water depth of the target area,

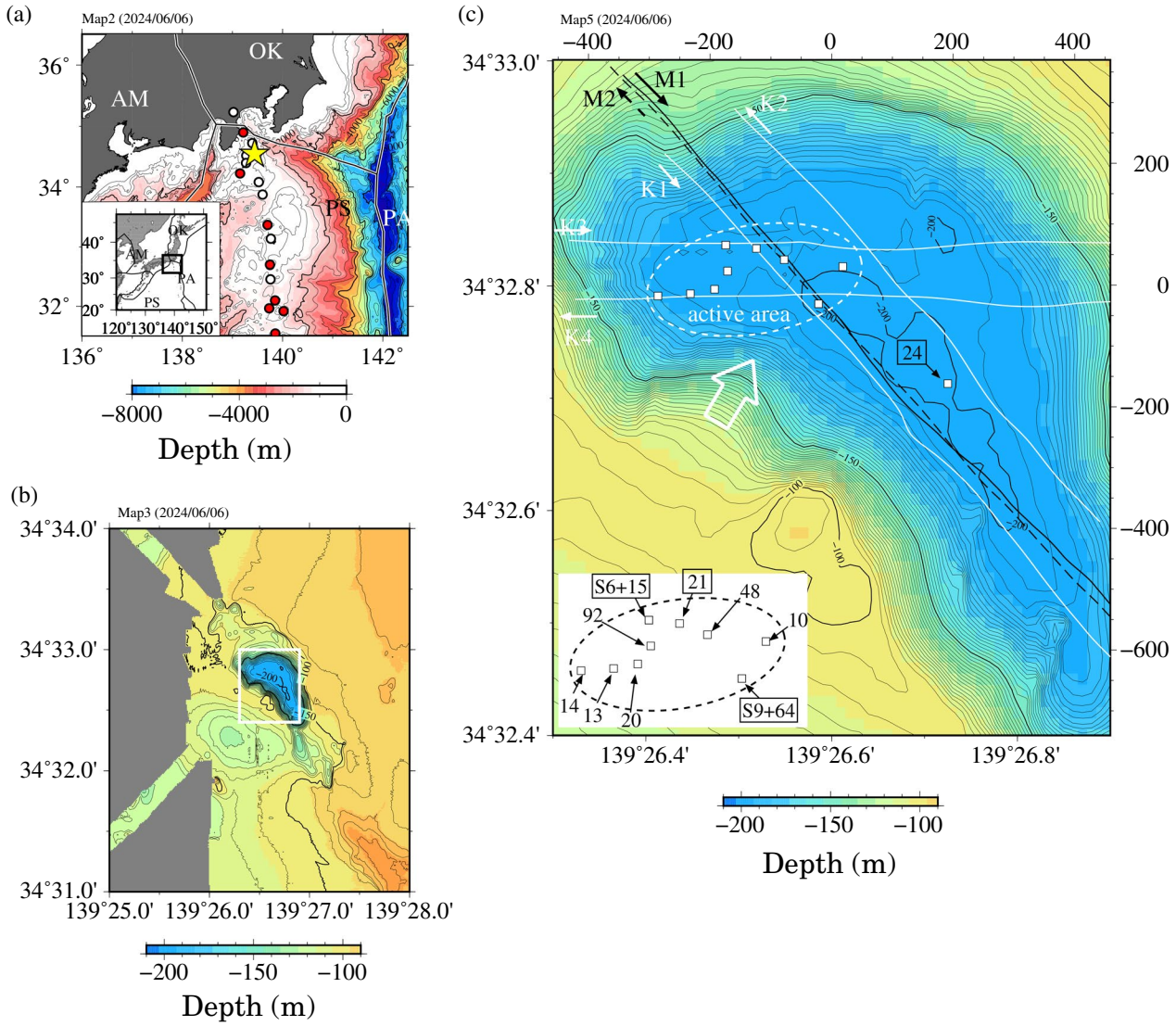

Fig. 1 Maps of the target area with survey lines and the locations of temperature sensors. The colour scale is given in the legend at the bottom of each map. **a** Izu-Ogasawara Arc with the filled circles (white for basaltic and red for dacitic to rhyolitic) corresponding to representative active volcanoes (Tamura et al. 2009; Honsho et al. 2016a). The location of Oomuro-dashi, which is classified as rhyolitic but contains a little basalt, is indicated by the yellow star. Plate boundaries are taken from Bird (2003). **b** Plan view of Oomuro-dashi volcano (a plateau-like surface) and its caldera structure. The square indicates the study area. **c** Close-up view of the study area corresponding to the white rectangle in **b** with the dive tracks (black and white curves), the locations of long-term bottom-water temperature measurements (open squares), and the hydrothermally active area (dashed ellipsoid). Sensor IDs are indicated by numbers in the inlet (not to scale) except for #24, one deployed outside the hydrothermal area. The numbers bounded by a box correspond to the sensors whose data are displayed in Fig. 8. The locations of the sensors and the hydrothermally active area are taken from Ohki et al. (2018). The white arrow indicates a kink in the caldera wall

and which may contain information on subsurface fluid flow. Because fluid flow may directly and indirectly influence the self-potential as mentioned above, the results are useful for interpreting the self-potential observations that cannot be explained by the original or vertical geobattery model, which does not take the effect of fluid flow into account. The following sections are organised as follows: geological setting of the study area; information on the scientific expeditions and methods of analysis; results of the self-potential and long-term temperature measurements; inverse modelling of the observed results; possible mechanisms to explain the observed results using numerical models; and concluding remarks.

2 Geological setting of the study area

The Izu-Ogasawara Arc, south of the main island of Japan, is formed by the westward subduction of the Pacific Plate (PA) into the Philippine Sea Plate (PS) (Fig. 1a). Volcanic islands and submarine volcanoes are aligned in a North–South direction on the Philippine Sea Plate (PS). Volcanoes composed of basalt and those composed of dacite or rhyolite are alternately located along the arc (red and white circles in Fig. 1a; Tamura and Tatsumi 2002; Tamura et al. 2009). Dacitic to rhyolitic volcanoes tend to form a caldera associated with explosive eruptions due to the high water content of such magmas (e.g. McBirney 1963). The target of the present study, Oomuro-dashi, is a submarine volcano of this type, although its chemical composition is bimodal, predominantly rhyolitic with some basalt (McIntosh et al. 2022).

Oomuro-dashi is a submarine volcanic province with a caldera hole at its summit (Hamuro et al 1983) (Fig. 1b). Volcanic eruptions may have formed a plateau-like structure with a diameter of 20 km and a water depth of ~ 100 m. A single-channel seismic survey has imaged a layered alteration structure of rhyolitic lava and pumice in the plateau-like structure (Tani et al. 2012; JAMSTEC 2012). This type of structure has been widely reported in dacitic and rhyolitic volcanoes (Urabe et al. 2005; Tsuru et al. 2008). A 0.5 km by 1.5 km D-shaped caldera, called Oomuro-dashi Hole, the target of the present study, is located at the top of the plateau (Fig. 1b). The major axis is elongated in a NW–SE direction, and the shape of the caldera shape looks like the letter 'D' being rotated 45° counter-clockwise. The caldera wall has a height of ~ 100 m; the caldera floor has a water depth of ~ 200 m. The rock of the caldera wall is rhyolite, and the caldera floor consists of fine sand (Tani et al. 2012). The caldera wall has a relatively gentle slope in its northeastern part (the rounded part of the letter 'D') and a steep slope on the opposite side (the linear part of the letter 'D'). The steep wall changes the strike from NW–SE in its southern part to E–W near the northwestern end (the white arrow in Fig. 1c). This may indicate a linear E–W trending subseafloor structure. Throughout this study, we use a bathymetric map of ~ 20 m resolution compiled from 50 kHz multi-beam echo sounder (MBES) data acquired by R/V *Natsushima* of the Japan Agency for Marine-Earth Science and Technology (JAMSTEC) during the expedition NT14-E02.

Hydrothermal activity (white-coloured seafloor, diffuse flow, hydrothermal vents and chimneys) has been observed in the northern part of the caldera floor (Ohki et al. 2018; dashed ellipsoid in Figs. 1 and 2 and coloured symbols in Fig. 2a), north of the inferred linear structure (white arrow in Fig. 1c). The hydrothermally active area, as defined by in situ temperature measurements on the seafloor (Ohki et al. 2018), extends 300 m and 150 m in the EW and NW directions, respectively (dashed ellipsoid in Fig. 2). Example photographs of less-active and active areas are shown in Fig. 2c and d, respectively. The distribution of seafloor temperature anomalies (> 50 °C) is concentrated in this active area (Ohki et al. 2018; Fig. 2b). The highest temperature of the discharged fluids is ~ 200 °C (Tani et al. 2012), which corresponds to the boiling temperature of seawater at a water depth of 200 m or a pressure of 2 MPa (Bischoff and Rosenbauer 1988). Small white chimneys were identified at three locations in the active area (red triangles in Fig. 2a). These chimneys are small (Fig. 2e), and some have collapsed and others will collapse before growing. Tubeworms and bacterial mats were commonly observed near active hydrothermal vents on the flat seafloor (Fig. 2f). Further example photographs can be found in Additional file 1: Figure S1.

Due to the shallow water depth (~ 200 m) and the Kuroshio current flowing near the target area (e.g. Mizuno and White 1983), the bottom-water temperature is expected to change with time. The subseafloor temperature thus provides information on the subseafloor flow velocity and the thermal properties of the sediment (Goto et al. 2005), as the information on temperature changes influenced by these properties diffuses downwards under these conditions.

3 Materials and methods

3.1 Equipment

We employed the same self-potential measurement system used in our previous studies (e.g. Kawada and Kasaya 2017). A 30-m-long fibre-reinforced plastic (FRP) sensor cable was connected to the tail of the deep-tow, on which five non-polarised Ag/AgCl electrodes (Filloux 1987), separated by 5 m and referenced to a common Ag/AgCl electrode, were mounted (Fig. 3). The electrostatic potential of each sensor was recorded by a high-precision (24-bit) high-impedance multichannel electrometer, which is a component of a marine electromagnetic

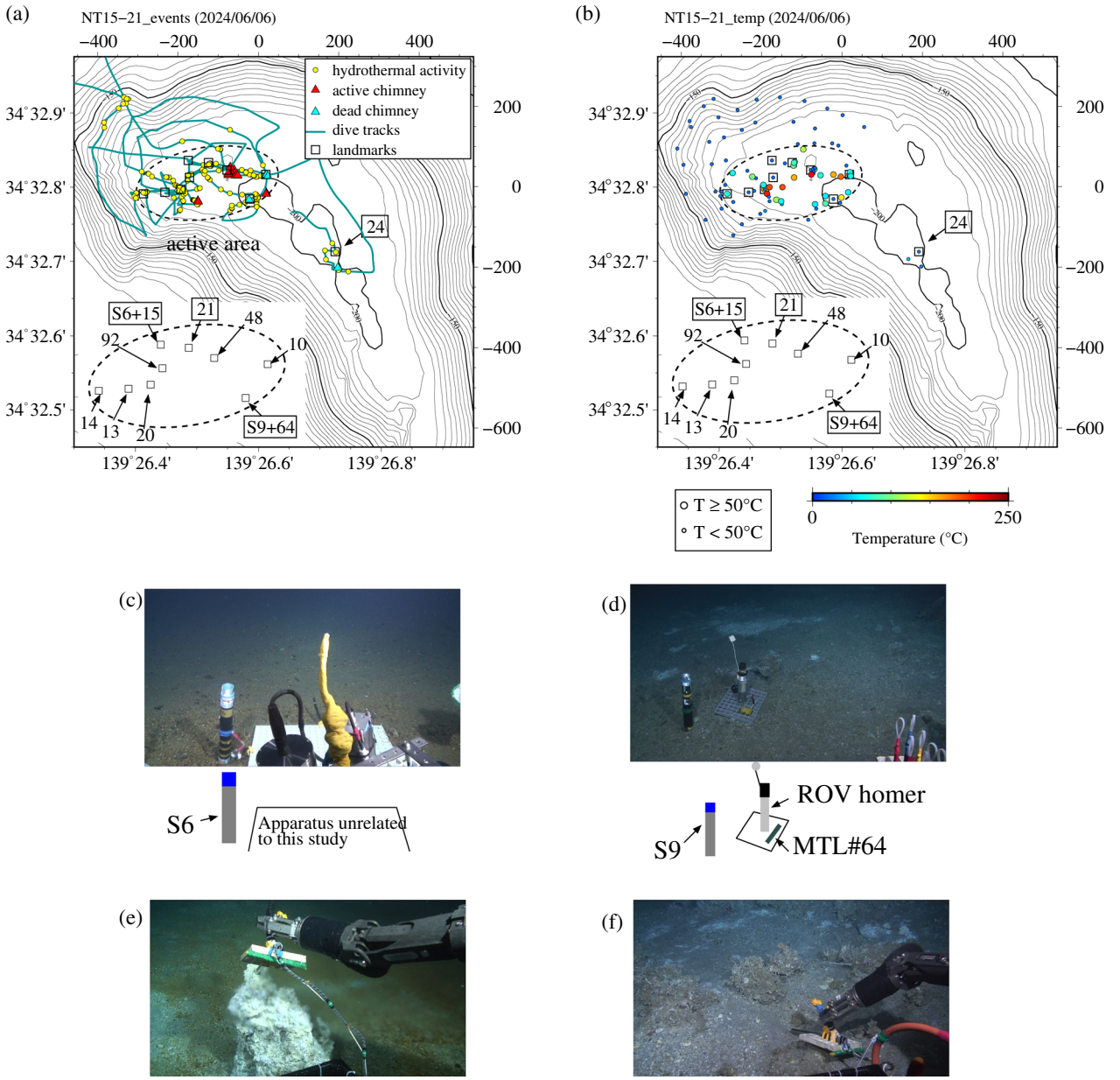

Fig. 2 Hydrothermal activity of the Oomuro-dashi Hole. Note that **a** and **b** use the same raw data as in Ohki et al. (2018) but newly drawn by the authors of the present paper. **a** Visible hydrothermal signatures (e.g. white-coloured seafloor; yellow circles), active chimneys (red triangles), and dead chimneys (blue triangles). The dashed ellipsoid represents the hydrothermally active area, which covers the area with seafloor temperatures above 50 °C. The dive tracks of the expedition NT15-21 are indicated by the grey curves, and the locations of the long-term bottom-water temperature measurements are denoted by the open squares. Sensor IDs are indicated by numbers in the inlet except for #24, one deployed outside the hydrothermal area. The numbers bounded by a box correspond to the sensors whose data are displayed in Fig. 8. **b** Temperature distribution at the seafloor with the colour scale shown in the legend. Temperatures below 50 °C are indicated by a small circle and those equal to or above 50 °C by a large circle. **c** Photograph for Station 15 with SAHF S6. The seafloor is sandy. **d** Photograph for Station 64 with SAHF S9. The seafloor is also sandy, but there are white-coloured spots behind the instrument. At the bottom of **c** and **d**, schematic diagrams explaining the instrument are added. **e** Photograph of a small hydrothermal chimney during temperature measurement. **f** Photograph showing tubeworms

survey system (Kasaya et al. 2019). The electrometer is capable of recording data at a maximum sampling rate of 1 kHz. Two acoustic transponders were attached for positioning, one at the deep-tow and the other at the tail end of the sensor cable. These positions were monitored by the mothership's super-short baseline (SSBL) system.

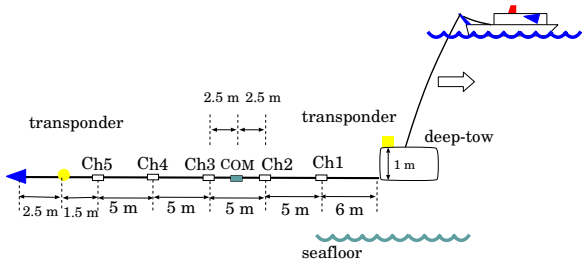

Fig. 3 Configurations of the self-potential measurement. The positions of five electrodes (white squares) and a reference electrode (a filled square) are shown along the FRP rod mounted on the deep-tow. The figure is modified from Kawada and Kasaya (2017)

Occasionally, a conductivity-temperature-depth (CTD) meter and an acoustic altimeter were mounted on the deep-tow.

Long-term monitoring of subseafloor and ambient bottom-water (near-seafloor) temperatures was carried out independently of the self-potential surveys. Two heat-flow probes named SAHFs (Stand-Alone Heat-Flow meters, manufactured by Kaiyo Denshi Co. Ltd.; Kinoshita et al. 2006) were used to record subseafloor temperature profiles on the hydrothermally active area. The SAHF has a 50-cm-long and 1-cm-diameter probe with five calibrated thermistors mounted at 11-cm intervals. Temperature records have a resolution of 0.001 °C. Ten commercially available small (15 mm diameter and 160 mm long) temperature loggers named MTLs (Miniaturised Temperature data Loggers, manufactured by ANTARES Datensysteme GmbH; Pfender and Villinger 2002) were used to monitor the bottom-water temperature at various locations on the caldera floor. They have a resolution of 0.001 °C.

3.2 Survey summary

Two expeditions, MR16-01 (2016/1/29–2016/2/7) by R/V *Mirai* and KM16-03 (2016/6/3–2016/6/10) by R/V *Kaimei* of JAMSTEC, were conducted in a known hydrothermal system (the Oomuro-dashi hydrothermal field) in the Oomuro-dashi Hole to investigate self-potential anomalies using a deep-tow system passively towed by the mothership. We have totally six survey tracks (Fig. 1c). During MR16-01, a round-trip survey was conducted along a line running from NW to SE and a line running from SE to NW (Line M2) along the almost identical path. During KM16-03, surveys were carried out along a line running from NW to SE (Line K1, which attempted to retrace Lines M1 and M2) and a line running from SE to NW (Line K2, 200 m east of Line K1). Surveys were also carried out along a line running from W to E (Line K3) and a line running along from E to W (Line K4, 100 m south of Line K3). The survey altitude was ~ 5 m, and the towing speed was ~ 1 knot (~ 0.5 m/s). Note that the expedition KM16-03 conducted an active electrical survey at the same time, but the results will be reported elsewhere and are not presented in this paper.

During both expeditions, in situ electrical potentials were recorded at a sampling rate of 50 Hz or more, but 1 Hz downsampled data were used for the analysis of the self-potential. The positions of the deep-tow and the tail of the cable were monitored by the SSBL system at 4-s intervals, allowing the cable angle to be estimated. The altitude was monitored by a video camera and an effort was made to keep the survey altitude at 5 m because the altimeter was not working (KM16-03) or not installed (MR16-01). The deep-tow altitude can later be estimated from the deep-tow position using the bathymetric map. During KM16-03, ambient temperature, electrical conductivity, and pressure were recorded by the CTD at 1-s intervals.

Two SAHFs, labelled S6 and S9, were respectively deployed on 2015/12/15 (S6) and 2015/12/14 (S9) during the expedition NT15-21 and retrieved on 2016/4/26 during the expedition KS-16-J06 (see Figs. 1c and 2 for deployment locations). We thus have 4.5 months of data with a sampling rate of 10 min. The deployment locations of S6 and S9 correspond to Sites H and J of Ohki et al. (2018), respectively. S6 was deployed near the northern edge of the hydrothermally active area, where there is no visible hydrothermal activity (Fig. 2c); S9 was deployed near the southern edge of the hydrothermal area, where there is a white-coloured seafloor (Fig. 2d). Both probes achieved vertical and full penetration (Fig. 2c and d). Ten MTLs were deployed broadly across the caldera floor (Figs. 1c and 2) to record ambient temperatures a few centimetres above the seafloor. These were mounted on equipment units for ranging (called ROV-Homer, manufactured by Sonardyne Inc.; Fig. 2d). The observation period of the MTLs is similar to that of the SAHFs, and the sampling rate was also 10 min. Note that 4 MTLs (10, 21, 24, and 92) were found lying down at the time of retrieval.

3.3 Data analysis

The 0.25 Hz (4 s interval) SSBL data for the positions of the deep-tow and the tail of the cable are interpolated to 1 Hz using the 'filter1d' and 'sample1d' commands of the Generic Mapping Tools (GMT; Wessel et al. 2019) to obtain the same sampling rate as the other components (1 Hz) and to deal with scattered and missing data. As the depths of the deep-tow and the tail of the cable were almost identical and in line, we assume that the sensor cable is parallel to the horizon and in line with the transect (see Additional file 1: Figure S2 for the cable

angle). The survey lines, named Lines M1–M2 and K1–K4 (Fig. 1c), are selected manually by picking up intervals where the deep-tow ran straight. We obtain the direction of these transects and the positions projected onto them using the 'project' command of GMT (Wessel et al. 2019).

The 1 Hz voltage data, downsampled from the original data of 50 Hz or more, are further processed through a 15-s-long cosine filter using the 'filter1d' of GMT (Wessel et al. 2019) to remove high-frequency noise (as well as signals of the electric sounding for the KM16-03 data). This procedure of reducing high frequencies is similar to that used in Constable et al. (2018). The subsequent analysis follows our previous studies (e.g. Kawada and Kasaya 2017, 2018). First, the data are clipped to each survey line. Then, for each survey line and each channel, both a constant offset and a linear trend with time are removed from the filtered data by subtracting the linear least-squares fitted data. Finally, the electric field and the self-potential are calculated.

Since each electric potential (V_i with i being the channel number of the sensor) is referenced to a common electrode, the electric field between the i-th (deep-tow side) and the j-th (tail side) sensors is written as.

$$E_{ij}^{\mathrm{obs}} = -\frac{V_i - V_j}{d_{ij}}, \tag{1}$$

which is calculated from the two electrostatic potentials V_i and V_j divided by the distance between the two electrodes d_{ij} and adding the minus sign. We have four *independent* electric fields using two adjacent sensors divided by the sensor distance of 5 m (Fig. 3). Assuming that the electric field is parallel to the survey line, the self-potential of any combination of sensors is approximately calculated by integrating the electric field along the line,

$$\phi_{ij}(l) = -\int_0^l E_{ij}^{\mathrm{obs}}(l')dl', \tag{2}$$

where l is the distance relative to an arbitrary position along the line. Here it is assumed that the self-potential at the reference point ($l = 0$) far from the target is 0, i.e., $\phi_{ij}(0) = 0$. For data visualisation, the reference directions are chosen (NW to SE and W to E) and the sign of the electric field is reversed when the survey direction is opposite to the corresponding reference direction. For each sensor pair, the horizontal position in the transect plot is shifted according to the sensor configuration (Fig. 3) so that the signals plotted in the figure point to the same location. For example, for the data acquired at the same time, the position where E_{23} is plotted is 5 m closer to the deep-tow than the position where E_{12} is plotted. Note that Ch. 1 (the one installed closest to the deep-tow; Fig. 3) did not function properly during KM16-03 and is excluded from the analysis (see Additional file 1: Figure S3 for the full data during KM16-03 including this channel).

The data of long-term subseafloor temperatures acquired by the SAHFs and a bottom-water temperature acquired by the MTLs are used as such for data visualisation. For estimating the Darcy velocity at the S6 and S9 sites, these data are processed through a 1-day-long cosine filter using the 'filter1d' of GMT (Wessel et al. 2019). In the present analysis, the bottom-water temperature recorded at the same station as S6 (Station 15) is used instead of the shallowest sensor, as the latter showed a large offset and drifts.

4 Observational results

4.1 Self-potential anomalies

A pair of positive and negative self-potential anomalies were observed around a hydrothermally active area (Figs. 4, 5, 6, 7). The negative part is located in the southern part of the hydrothermally active area (dashed circles in Figs. 2, 4, and 6), characterised by the presence of hydrothermal signatures (e.g. white-coloured seafloor, hydrothermal chimneys, and tubeworms) and high seafloor temperatures (> 50 °C; Ohki et al. 2018). The positive counterpart is located in the northern part of the active area, also characterised by high seafloor temperatures. Thus, the area of the self-potential anomalies, the sum of the positive and negative areas, basically coincides with the hydrothermally active area defined by the measurement of seafloor temperatures (Figs. 4 and 6). However, the positive part also extends further north and northeast of this active area (outside the dashed ellipsoid in Figs. 4 and 6). The magnitude of the positive and negative self-potential anomalies (Upper panels in Figs. 5 and 7), calculated from the horizontal electric field being integrated along the survey line, is of the order of 1 millivolt at the survey height of ~ 5 m.

The pair of positive and negative self-potential anomalies were encountered three times at almost the same location. During the expedition MR16-01 (Figs. 4 and 5), the pair was observed twice by a round-trip survey along two lines following almost the same track in opposite directions (Line M1 running from NW to SE, Fig. 5a; Line M2 running from SE to NW, Fig. 5b). Lines M1 and M2 give essentially identical self-potential patterns, although the amplitudes are slightly different between the lines and between pairs of sensors. Thirdly, during the expedition KM16-03 (Figs. 6 and 7), this paired self-potential anomaly was again detected along with Line K1 (from NW to SE; Fig. 7a). In all these three lines, the sign of the horizontal electric field changes at least three times along the lines, and the electric field has the same

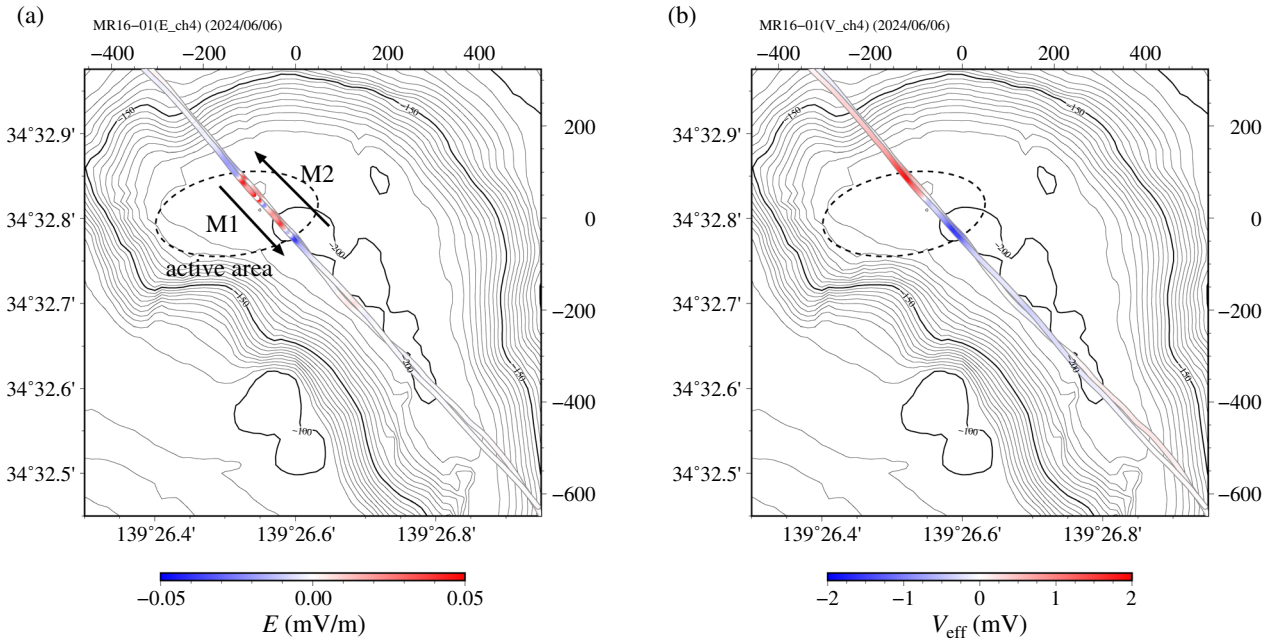

Fig. 4 Plan view of the results obtained during the expedition MR16-01. **a** The electric field in mV/m; and **b** the *effective* self-potential in mV. The colour scale is given in the legend at the bottom of each panel. The electric field is basically in the horizontal direction. The letters are the line numbers corresponding to Fig. 1c. The arrows correspond to the survey direction. The dashed ellipsoid is the hydrothermally active area identified by Ohki et al. (2018)

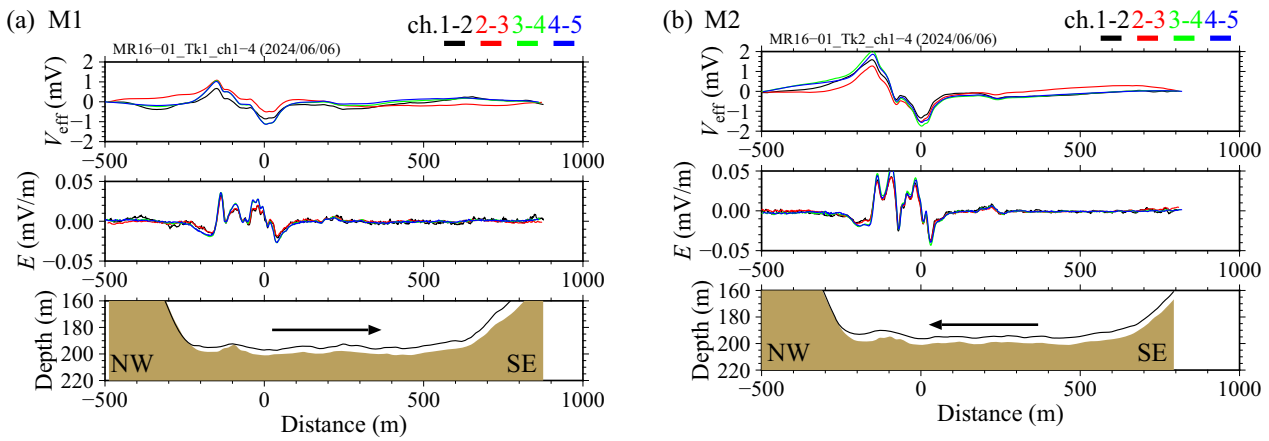

Fig. 5 Cross-sectional view of the results obtained during the expedition MR16-01. **a** Line M1 and **b** Line M2. The location of the lines is shown in Fig. 4. (Upper) The *effective* self-potential (solid curves, whose colour refers to the legend at the top), (Middle) the electric field (solid curves, colour refers to the legend above the figure), and (Lower) the survey altitude (black curves) and the bathymetry (the top of the brown area) with the survey direction indicated by the arrow. The electric field is basically in the horizontal direction. Note that this bathymetry was estimated using the previously obtained bathymetric contour map, and there is no record of ambient temperature (of the CTD meter) during this expedition

sign at its entry and exit (compare the middle panels of Fig. 5a and b with that of Fig. 7a). Thus, the pair of negative and positive self-potential anomalies *must* exist. It should be noted that small-spatial-scale variations in the electric field can be reproduced between these three survey lines.

Only one of the positive or negative parts of the pair was observed separately along the other survey lines of the expedition KM16-03. The positive part of the pair was possibly detected along Line K3 running from E to W (Fig. 7c), where it crosses Lines M1, M2, and K1. Another discrete positive self-potential anomaly was observed

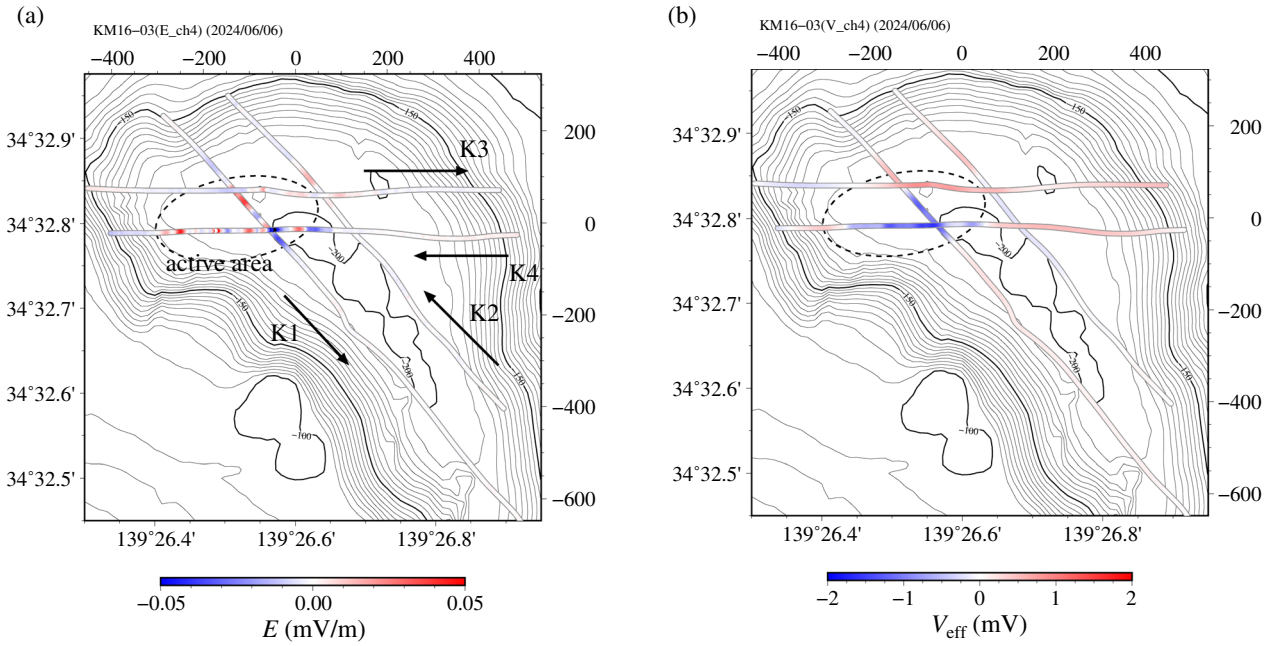

Fig. 6 Plan view of the results obtained during the expedition KM16-03. **a** The electric field in mV/m and **b** the *effective* self-potential in mV. The notation follows Fig. 4. The electric field is basically in the horizontal direction

along with Line K2 (Fig. 7b). The line encountered the positive anomaly 200 m northeast of the hydrothermally active area, suggesting that the positive anomaly has its northern extension outside the active area. The negative part of the pair was observed along Line K4 running from W to E (Fig. 7d), where it crosses the active part of the hydrothermal area. The sign of the horizontal electric field changes many times along with the eastern part of Line K4, indicating the presence of small spatial-scale structures along the line.

4.2 Variations of ambient water and subseafloor temperatures

Water temperature near the seafloor varied uniformly across the caldera floor (see grey curves in Fig. 8), indicating the presence of large-scale (caldera-scale) water movements (see Fig. 1c or 2 for the deployment locations). MTLs deployed away from the hydrothermal area (Station 24; Fig. 8a) and those deployed within the hydrothermally active area (Stations 21, 15, and 64; Fig. 8b and grey curves labelled #15 and #64 in Fig. 8c and d) recorded essentially the same temperature variations. The temperature changed by ~ 5 °C during the observation period. The MTL deployed at Station 21 (Fig. 8b), where the positive self-potential anomaly was observed, showed a relatively large noise. This MTL, which was found lying down on retrieval, may have suffered from intermittent fluid discharge. However, other MTLs deployed above the hydrothermally active area (i.e. Stations 15 and 64; grey curves in Fig. 8c and d) do not show such significant noise, although some of them were also lying down. See Additional file 1: Figure S4 for other bottom-water temperatures.

The observed subseafloor temperature profiles contain some signatures of hydrothermal activity, although the responses differ between the deployed two SAHFs. One, S6, deployed at Station 15 near the northern edge of the hydrothermally active area with the observed positive self-potential anomaly (Figs. 4 and 6) but no visible hydrothermal activity (e.g. Fig. 2c), shows gradual changes in the temperature with depth. The temperatures in Fig. 8c are the pre-filtered raw data (with the shallowest sensor, Ch. 5, showing erroneous deviations from the others). High-frequency components of the temperature variations gradually decrease with depth, and the phase of the temperature changes is delayed with depth (Fig. 8c; the sensor geometry is shown in Fig. 8e). This is a typical pattern in the presence of water temperature variations propagating downwards (e.g. Hamamoto et al. 2005). Analysis is required to determine whether fluid flow is present.

The other, S9, deployed at Station 64 near the southern edge of the hydrothermal area with the negative self-potential anomaly (Figs. 4 and 6), dominates the higher-frequency components for all sensors (temperatures in Fig. 8d are the pre-filtered raw data), reflecting the intense hydrothermal activity (e.g. Figure 2d). The variations of the shallowest sensors of S9 are similar to

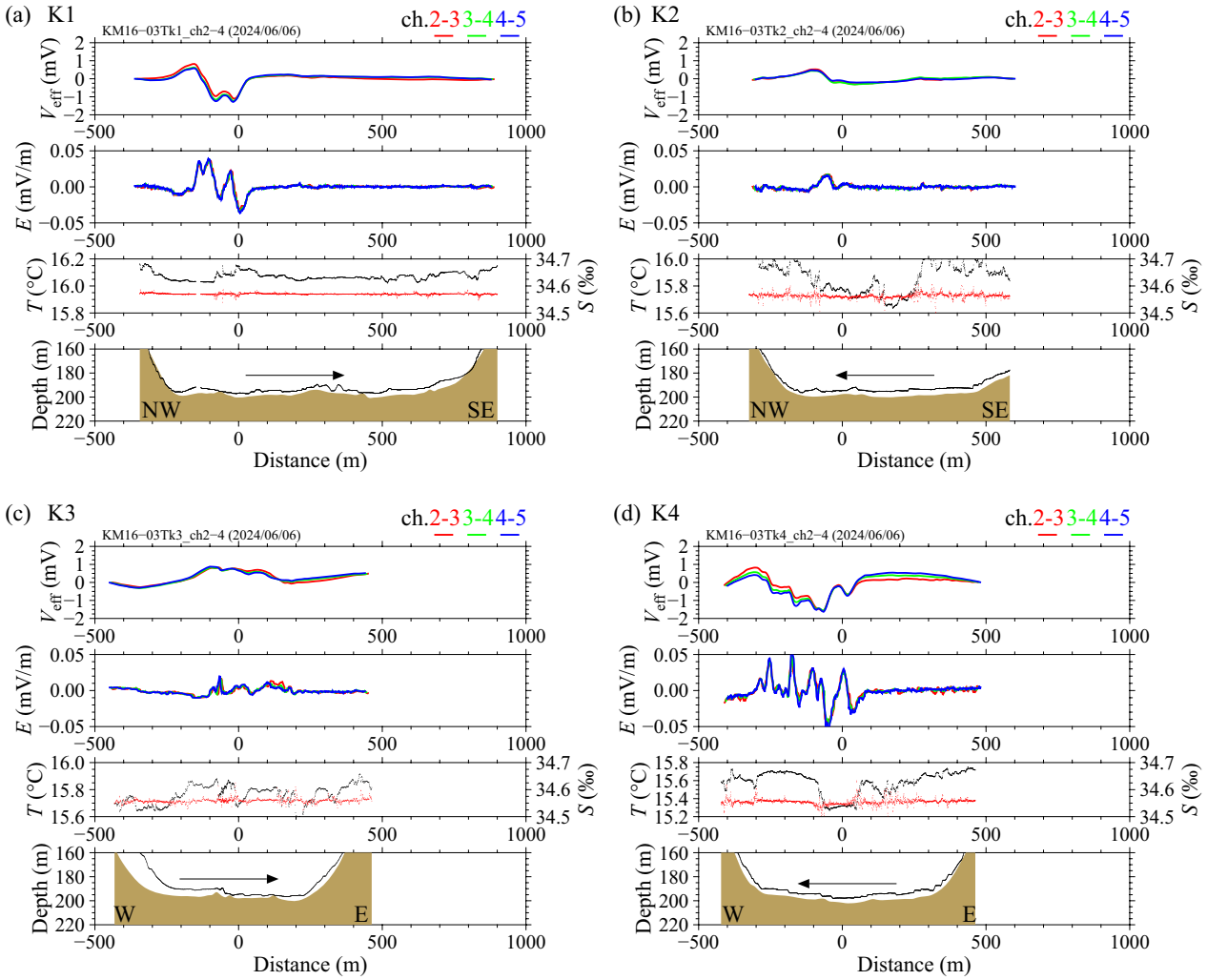

Fig. 7 Cross-sectional view of the results obtained during the expedition KM16-03. **a** Line K1, **b** Line K2, **c** Line K3, and **d** Line K4. The location of the lines is shown in Fig. 6 with the line name. (Top) The *effective* self-potential, (Upper middle) the electric field, (Lower middle) the ambient temperature (black dots) and salinity (red dots) observed by the CTD meter attached to the deep-tow system, and (Lower) the survey height and bathymetry. The electric field is basically in the horizontal direction. Note that the depth of the survey track is obtained using the pressure meter, as the vertical component of the SSBL system did not work well during this expedition. The notation follows Fig. 5

those of the bottom-water temperature (grey, magenta, blue, and green curves in Fig. 8d). The temperatures of the three shallower sensors increase regularly with depth, but the variations for the two deeper sensors appear to be in phase (black and red curves in Fig. 8d). The two deepest sensors have higher temperatures and large amplitude variations that cannot be explained simply by the downward propagation of seafloor temperature variations.

5 Inverse modelling of the results

5.1 Source estimation for the self-potential anomalies

To interpret the paired self-potential anomaly, we perform a 2.5-dimensional simplified current source inversion on the electric field data. Because the conductivity structure has not been obtained in the study area, we assume a homogeneous electrical conductivity. Although the exact burial depth and the extent of anomalous bodies may be influenced by the conductivity structure, the existence of current sources at depth can be well distinguished without the detailed conductivity structure (e.g. Zhu et al. 2020). Our method is similar to the one developed by Minsley et al. (2007), except that we use the analytical electric field for a point current source in homogeneous space instead of calculating the Green's function using the conductivity structure of the target area. The observed electric field is represented as the sum of the electric fields from point electrical current sources along with a vertical plane below the observation

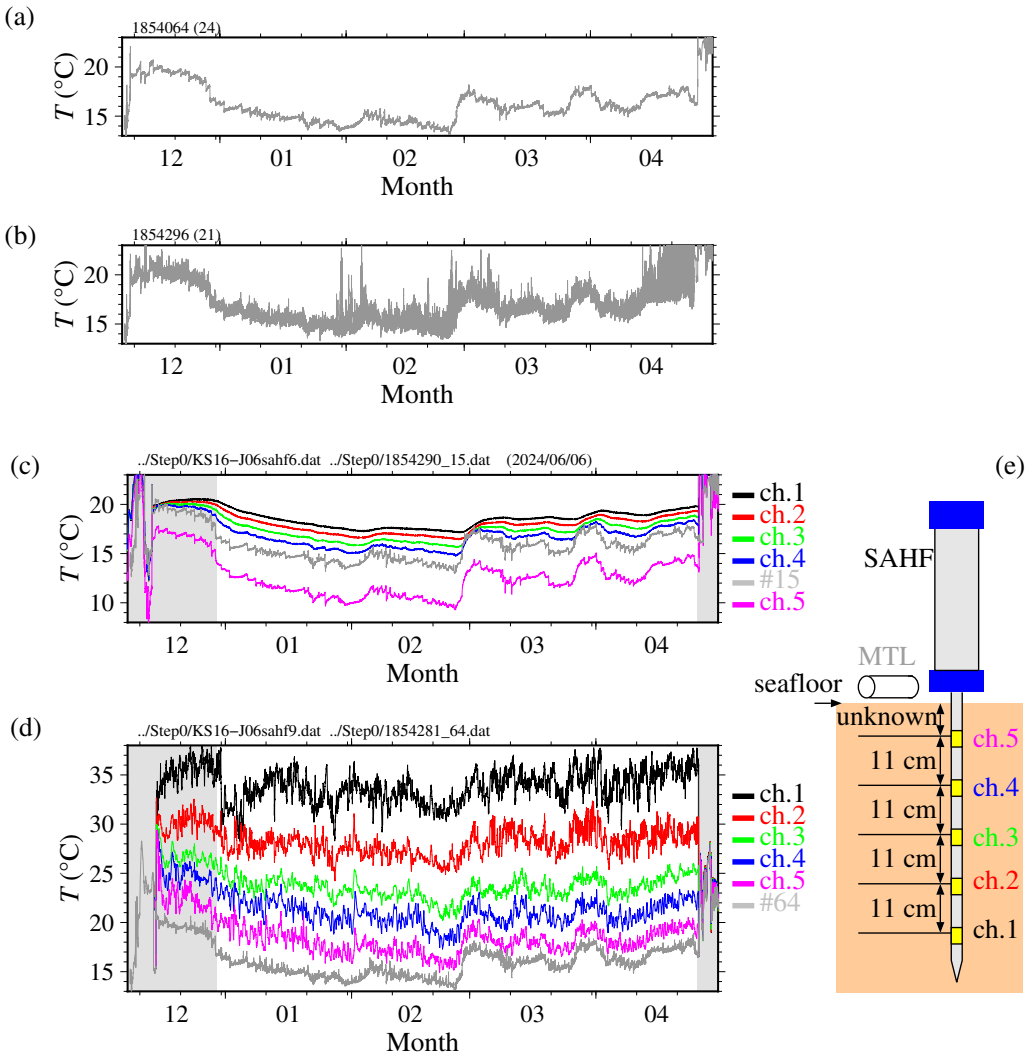

Fig. 8 Selected time series for temperature sensors. **a** Bottom-water temperature observed by an MTL at Station 24 outside the hydrothermal area. **b** Bottom-water temperature at Station 21 inside the hydrothermally active area. **c** Sub-seafloor temperatures observed by a 5-channel heat-flow probe (SAHF) S6 at the northern edge of the hydrothermal area (coloured curves) and the bottom-water temperature at Station 15 near the probe (grey curve). Note that Ch. 5 of S6 (near the seafloor; purple curve) did not work well. **d** Subsurface temperatures observed by a heat-flow probe S9 near the southern edge of the hydrothermal area and the bottom-water temperature at Station 64 near the probe. **e** Schematic sensor configuration of the heat-flow probe. See Figs. 1c and 2 and Additional file 1: Figure S1 for the deployment locations

line. The misfit between the observed and synthetic electric fields is optimised using the L_1-norm constrained (or sparse) least-squares method (e.g. Sugiyama 2013) and is regularised by the L-curve method (e.g. Hansen 2001). See Additional file 2: Appendix A for details of the method. We assume that the background medium has an electrical conductivity of 3 S/m, an arithmetic mean of the seawater conductivity of 5 S/m and the sediment–seawater conductivity of 1 S/m. The analysis in Additional file 2: Appendix B shows that these two cases are equivalent in terms of the source intensity.

We focus on Line M1 of MR16-01, which crosses both the negative and positive self-potential anomalies (Fig. 5a). We chose this survey line because the data are not contaminated by the electrical survey signals. The input data is the electric field (Ch. 4 vs. 5) along the track, and its direction is assumed to be horizontal. The model fits the data (horizontal electric field) to determine the source strength at specified locations (separated by 10 m horizontally and 4 m vertically at and below the seafloor level). The number of data is 1279 (the data along ~ 600 m of the survey line are used), and the number of sources

is 1891. The optimisation procedure minimises the sum of the L_2-norm of the model misfit and the L_1-norm of the model coefficients (source strengths), and the relative importance is controlled by a hyperparameter λ (a coefficient of the L_1-norm term). The best hyperparameter is found where the curvature is the maximum via the L-curve method (e.g. Hansen 2001). We ran the model with various λ's to obtain the optimal value.

In the best model (Fig. 9a), where the L-curve has the maximum curvature (Fig. 9b and c), a paired current source is imaged. A ~25-m-deep ($z = -225$ m below the sea level) negative current source is predicted at $x = 0$ m in the horizontal direction (N_1 in the lower panel of Fig. 9a; the origin of the horizontal axis is arbitrary), above which the negative self-potential was observed; a ~30-m-deep ($z = -230$ m) positive current source is predicted at $x = -150$ m (P_1 in the lower panel of Fig. 9a), above which the positive self-potential was observed. The current source pair forms a horizontally elongated dipole-like structure (see a schematic picture in the lower panel of Fig. 9a; its geological interpretation is given in the *Discussion*). Thanks to the L_1-norm constraint, most of the sources become close to 0. Other small negative and positive sources (e.g. p's and n's in Fig. 9a) are also imaged around the major current source pair, which are responsible for the small-scale self-potential anomalies. The maximum amplitude of the N_1 and P_1 is ~1.5 A, and the dipole moment is ~225 A m, if we take the distance between the positive and negative anomalies as 150 m.

Results with different λ's show that the fitting is not sensitive to λ, and plausible parameter values may range about one order of magnitude (Fig. 9c). Overfitting cases with large λ's concentrate the source near the seafloor (see Fig. 9d for an example of this type), while underfitting cases with small λ's locate sources similar to those of the best case (Fig. 9e, which is comparable to Fig. 9a). The underfitting case approximates the data well with a pair of positive and negative current sources.

5.2 Estimation of the Darcy velocity

The vertical Darcy velocity is estimated for the S6 data using the method of Goto et al. (2005). This method uses two temperature time series obtained at two different depth levels. One is obtained at a deeper depth level; the other is obtained at a shallower depth level but evaluated at the deeper depth level using the one-dimensional advection–diffusion equation with the vertical Darcy velocity and the thermal conductivity as parameters. The sensor geometry is shown in Fig. 10a. By taking any two from the five subseafloor temperature records (from a SAHF) and one bottom-water temperature record (from an MTL), the averaged Darcy velocity and the thermal conductivity between each pair can be estimated. Further details are given in Additional file 2: Appendix C.

The analysis uses the data between 2015/12/30 0:00 and 2016/4/25 23:50. We exclude the first 2000 points (~14 days for the sampling rate of 10 min) from the analysis (shaded area in Fig. 8c) because the data before the thermal diffusion time of 0.65 m with a thermal diffusivity for the sediment–water mixture of $\sim 3 \times 10^{-7}$ m^2/s may suffer from post-deployment disturbances. The analysis uses the 1-day-filtered data of the unshaded area in Fig. 8c, from which further 2000 points are excluded from the misfit calculation to avoid including early-stage perturbations. See Additional file 1: Figure S5a for the smoothed data.

The analysis of S6 predicts a downward Darcy velocity of $\sim 3 \times 10^{-7}$ m/s or ~9 m/yr (Fig. 10b) with a thermal conductivity of 1−1.5 W/m/K increasing with depth (Fig. 10c). The thermal diffusivity and the *effective* Darcy velocity, both of which include the effects of material properties and are more primitive data in the analysis, can be found in Additional file 1: Figure S5. The estimated Darcy velocity, which excludes the effects of material properties, is almost independent of the choice of channels, except when the bottom-water temperature is used. When the bottom-water temperature is used, the penetration depth of 150 mm for Ch. 5 gives a better fit. The misfit does not become very large even for a case with forced zero velocity, but it is more plausible to keep a downward velocity because zero velocity predicts a thermal diffusivity that is too large for ordinary sediments (e.g. 8×10^{-7} m^2/s; Additional file 1: Figure S6). This type of trade-off occurs because both the increase in the downward velocity and the increase in thermal diffusivity cause a rapid transfer of information downwards. However, the inclusion of the Darcy velocity can reduce the misfit bias in the time series (Additional file 1: Figures S6 and S7). Note that the temperature profile shows a linear trend with depth (Fig. 10d), which is explained by a balance between the increase in the thermal conductivity with depth (making the profile concave upwards) and the decrease in the downward velocity (making the profile convex upwards). This characteristic cannot be extracted from time-averaged temperature profiles. Finally, using the time-averaged temperature, the temperature gradient at this station is estimated to be 6.2 K/m, at the penetration depth of 150 mm for Ch. 5, and the heat flow is then estimated to be 7.8 W/m^2 using a thermal conductivity of 1.25 W/m/K (Fig. 10c).

A different strategy is implemented for the S9 data (which has common temperature variations among all sensors and is not suitable for the above analysis) to estimate the vertical Darcy velocity. The time-averaged

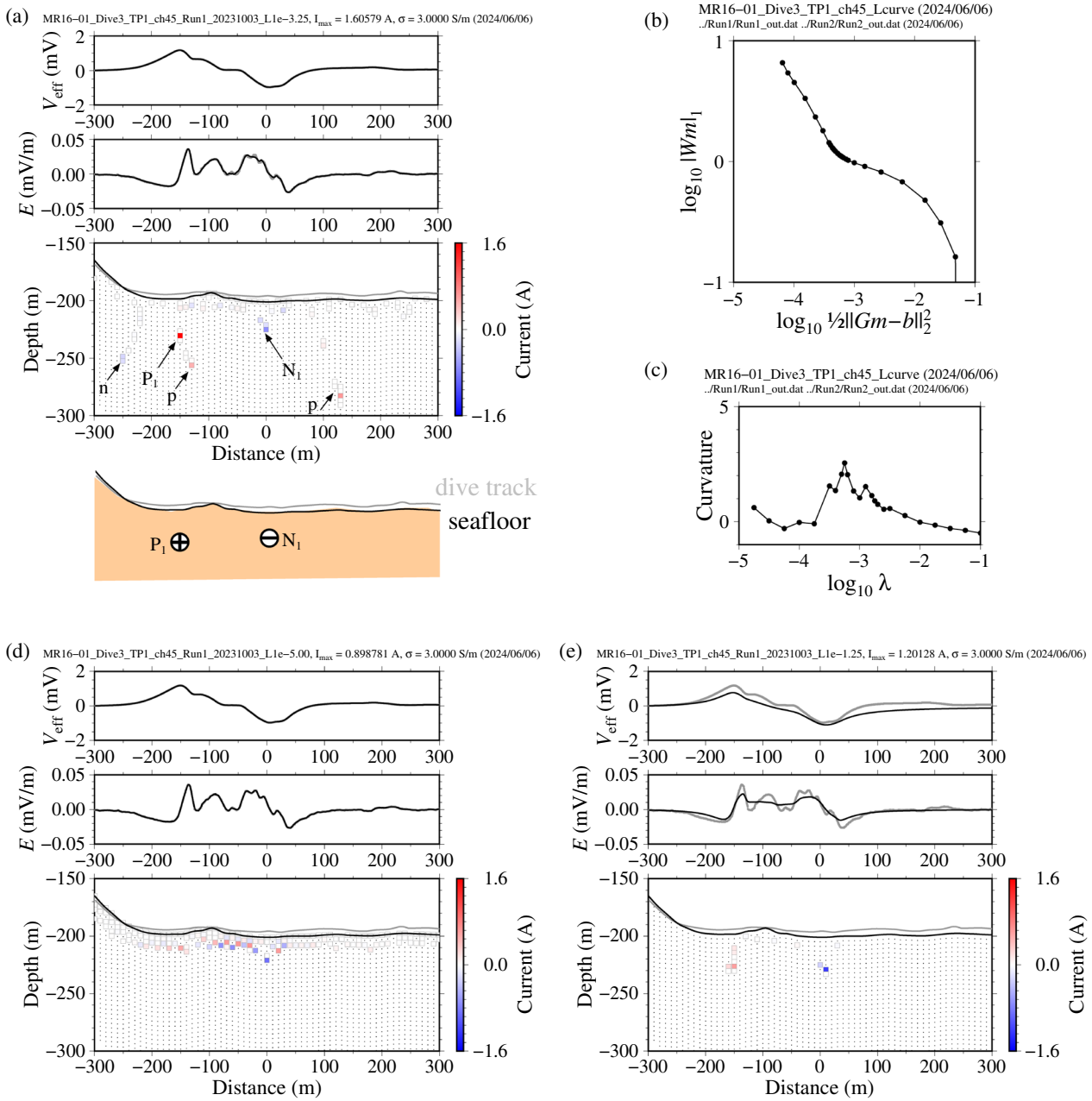

Fig. 9 Results of the simplified source inversion for Line M1. The electric field constructed by Ch. 4 and Ch. 5 (sensor pair farthest from the deep-tow; Fig. 3) is used. **a** Best result with $\lambda = 10^{-3.25}$. (Upper panel) The *effective* self-potential, obtained by integrating the horizontal electric field with the distance and adding the minus sign, corresponding to the input (observed; grey curve) and the output (modelled; black curve). The self-potential is not the input for the model. (Middle panel) The electric field of the input (observed; grey curve) and the output (modelled; black curve). The electric field is basically in the horizontal direction. The grey and black curves overlap almost completely in the upper and middle panels. (Lower panel) The inverted source strength at prescribed locations with a schematic cartoon (not to scale) at its bottom. The black curve indicates the seafloor, while the grey curve indicates the survey track. The seafloor itself does not affect the result as the resistivity is assumed to be constant, but the source locations are constrained below this curve. The red and blue squares denote positive and negative current sources (see the colour scale on the right). P_1 and N_1 are the major positive and negative current sources (~ 1.5 A), and p and n are other positive/negative sources. The dots show the sources whose amplitude is less than 10^{-10} A. Note that the track in the northeastern part (left side of the figure) is below the seafloor depth, which may be due to positioning errors. However, this does not affect the result as we have had almost no signal there. **b** The *L*-curve at various λ's, with the horizontal and vertical axes indicating the misfit and the effective amplitude, respectively. **c** The curvature of (**b**) as a function of λ. **d** An overfitted case with $\lambda = 10^{-5}$. The sources are concentrated near the seafloor. The grey and black curves overlap almost completely in this case. **e** An underfitted case with $\lambda = 10^{-1.25}$. A small number of sources can fit the main feature of the observation but the fine-scale features cannot be explained. Nevertheless, the source positions are similar to those in the best case (**a**)

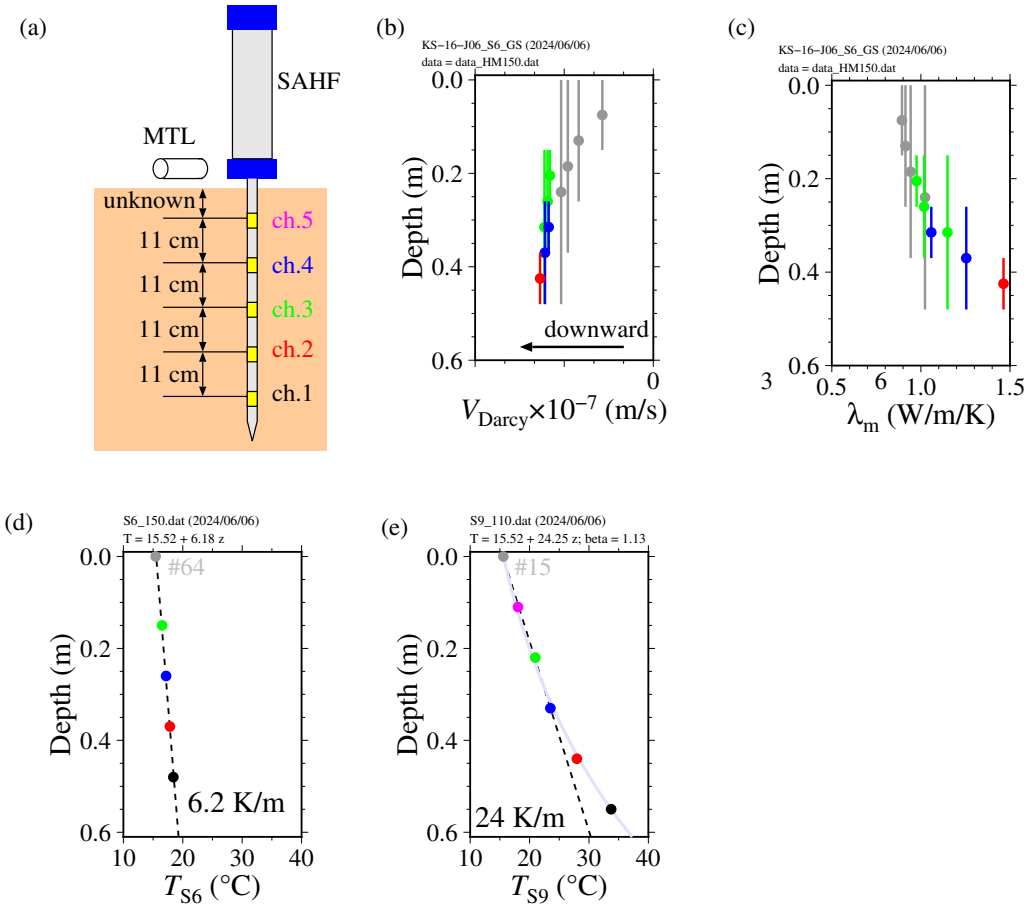

Fig. 10 Estimated Darcy velocity, thermal conductivity, and hypothetical undisturbed temperature profile. **a** Schematic sensor configuration of the heat-flow probe. The depths of the Ch. 5 sensor for S6 and S9 are unknown but assumed to be 150 and 110 mm, respectively, in the analysis, which give better results. **b** Reconstructed Darcy velocity and **c** thermal conductivity for S6 as a function of depth, which are the results of time-series inversion. The colours correspond to the shallower sensors in (**a**). **d** The temperature profile of S6 as a function of depth. The dashed line shows the least-squares fitted temperature gradient. **e** Same as (**d**) but for S9. The light blue curve shows the fit of the one-dimensional advective–diffusive solution of Bredehoeft and Papadopulos (1965). See Figs. 1c and 2 for the deployment locations

temperature profile is compared directly with analytical solutions of the steady-state advection-diffusion equation with non-linear temperature profiles with depth (Bredehoeft and Papadopulos 1965). The profile depends on the flow velocity. In short, convex upward (concave upward) temperature profiles predict upward (downward) flow. The details of the method are given in Additional file 2: Appendix D.

When the temperature fluctuations are averaged over the observation period, the temperature gradient between the three shallower sensors (Ch. 3 to 5) is 24 K/m (Fig. 10e). The penetration depth of 110 mm for Ch. 5 gives a better fit. The temperature gradient shows a 'kink' at mid-depth. Consider two situations to interpret this. First, assume a hydrothermal pool structure (Urabe et al. 2005) at a few tens of centimetres below the surface, but no fluid flow. Using the temperature gradient obtained from the three shallowest sensors and the thermal conductivity for S6, 1.25 W/m/K, the heat flow at S9 is estimated to be 30 W/m^2 (Fig. 10e), an order of magnitude greater than that at S6. Second, we use the temperature profile explicitly. When the kinked temperature gradient is fitted to the analytical solution of the one-dimensional advection–diffusion equation to estimate the Darcy velocity (Bredehoeft and Papadopulos 1965), the estimated velocity is downward, the magnitude of which is $\sim 8\times10^{-7}$ m/s or ~ 25 m/yr using the thermal conductivity of 1.25 W/m/K (Fig. 10c). This downflow at the S9 site is three times faster than that at the S6 site, possibly reflecting the hydrothermal activity at these sites. However, this may be an underestimate because the thermal conductivity variations with depth have not been taken into account (See discussion for the S6 data, where a slow downward flow is estimated but the time averaged

temperature profile shows a linear trend). We conclude that the S9 site is more active than the site S6, which is consistent with previous visual observations (Fig. 2; Ohki et al. 2018).

6 Discussion

The small amplitude of the observed self-potential, of the order of 1 millivolt at the survey height of ~5 m for both negative and positive signs (Figs. 4–7), combined with the results of the visual surveys suggests that there are no very large ore bodies beneath the seafloor in the Oomuro-dashi hydrothermal field. The observed self-potential is considerably smaller than that observed at a hydrothermally active area with massive sulphide structures, e.g., of the order of −100 mV at a survey height of ~5 m at the Izena hydrothermal field in the mid-Okinawa Trough (e.g. Kawada and Kasaya 2017) with large ore bodies confirmed by deep-sea drilling (METI 2013), or −70 mV at a survey height of ~ 70 m at another hydrothermal field in the mid-Okinawa Trough (e.g. Constable et al. 2018). The present results are more comparable to those observed in a less-active hydrothermal system in the Mediterranean Sea (e.g. Safipour et al. 2017) if only the magnitude of the self-potential anomalies is considered. The Oomuro-dashi hydrothermal field is active but lacks large sulphide structures above the seafloor according to camera surveys (Tani et al. 2012; JAMSTEC 2012; Ohki et al. 2018; Fig. 2). This field evidence is consistent with the thermodynamic perspective that the formation of large hydrothermal ore deposits requires great water depths (>2000 m) for the circulating fluid to reach high temperatures (>300 °C) to dissolve ore-forming chemical species (e.g. Ohmoto 1996). However, at present, there is no direct evidence of whether such ore bodies are present or absent *below* the seafloor in the Oomuro-dashi hydrothermal field.

What is significant is that, regardless of the presence or absence of large ore deposits, the previously observed self-potential anomalies are mostly negative. The negative self-potential anomaly has been explained by the geo-battery mechanism (Sato and Mooney 1960). The geo-battery involves chemical reactions occurring around an ore body with high electrical conductivity in the presence of a redox front and predicts a negative self-potential anomaly in an oxidised or high-Eh region and a positive self-potential anomaly in a reduced or low-Eh region. Thus, a horizontal redox front that becomes more reducing with depth results in the negative self-potential anomaly above the seafloor (Fig. 11a). The vertical geo-battery is represented by a downward electrical current dipole. On the other hand, a pair of negative and positive self-potential anomalies with similar amplitudes may indicate the presence of a horizontally elongated, or lying down, electric current dipole along the transect, with positive and negative current sources being located beneath the observed positive and negative self-potential anomalies, respectively (see the upper and lower panels in Fig. 8a). We therefore consider possible mechanism(s) for the observed paired self-potential anomaly. These are the horizontal geo-battery and the thermal/streaming potentials.

6.1 Horizontal geo-battery model

The horizontal geo-battery model, in which a conductive body lies across a non-horizontal redox front (Fig. 11b), is the first candidate to explain the observation of a pair of positive and negative self-potential anomalies (e.g. Fig. 4). The result of the source inversion (Fig. 9) can look like the original geo-battery of Sato and Mooney (1960) (Fig. 11a) lying horizontally (Fig. 11b). In this model, the low-Eh part of the geo-battery that accounts for the positive self-potential anomaly, which is buried at depth and invisible in the vertical geo-battery, is exposed near the seafloor and easily accessible. In addition, a conductive body lies beneath both the positive and negative self-potential anomalies.

To quantify the above intuition, a three-dimensional conceptual geo-battery model, similar to previous models (Bigalke and Grabner 1997; Castermant et al. 2008; Ishido et al. 2013), is constructed using a general-purpose FEM software, *COMSOL multiphysics*. The model is modified from a demonstration 'galvanized nail' of the software (COMSOL 2016). The computational domain consists of a sediment layer with 1000 m by 1000 m in the horizontal directions and 300 m in the vertical direction covered by a 200-m-thick layer of seawater. At the surface of a buried electrode in the sediment layer, the oxidation of iron (an anodic reaction) mainly occurs in the reduced part, and the reduction of oxygen (a cathodic reaction) mainly occurs in the oxidised part, respectively. In this study, the redox distribution is prescribed (Fig. 12a and b) by decreasing the rate of the cathodic reaction in the reduced part. The surface area involved in chemical reactions is set the same as the surface area of the solid conductive body. See Additional file 2: Appendix E for the details of the modelling and all parameter values used in the calculations. The parameter values (Additional file 2: Table E1) are not tuned for the marine geo-battery, as the purpose of the modelling here is rather to demonstrate how the distribution of the redox potential changes the resulting self-potential anomaly in the ocean.

The geo-battery can be divided into two end-member cases as explained above: horizontal and vertical. The first case corresponds to the vertical geo-battery for previous observations with negative self-potential anomalies (Fig. 11a). In this case, a cube of 40 m long in each

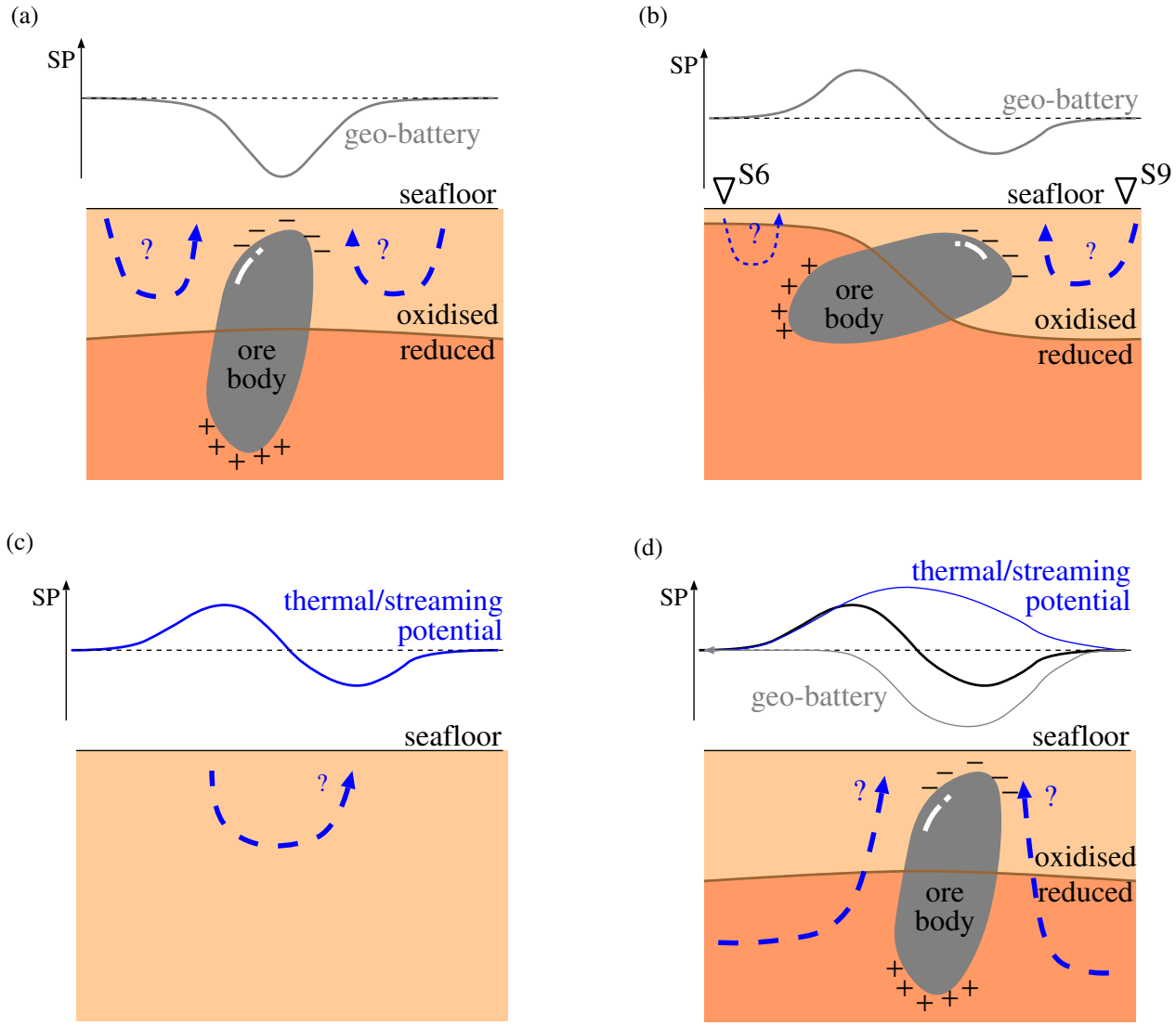

Fig. 11 Schematic representation of marine geo-batteries and the thermal/streaming potentials. (Upper) Expected self-potential anomaly at the seafloor; (Lower) a hypothetical subsurface structure. **a** The original or vertical geo-battery model of Sato and Mooney (1960), modified for the marine environment, in which a conductive body crosses a subseafloor redox horizon. **b** A horizontal geo-battery model, in which a subhorizontal conductive body crosses a disturbed or sub-vertical redox front. A conductive body is found below both the positive and negative anomalies. The inverted triangles correspond to the locations of SAHF S6 and S9 based on the results of the Darcy velocity estimation and the assumption that the strong convection deepens the redox horizon. **c** Thermal/streaming potentials model, where both positive and negative self-potential anomalies solely result from these potentials. This model requires no conductive body. **d** Mixed model, where the vertical geo-battery is responsible for the negative anomaly, and the thermal/streaming potentials contribute to the positive anomaly. A conductive body is expected only below the negative anomaly

direction is placed below the seafloor, with the top 10 m below the seafloor and the horizontal redox front crossing 30 m below the seafloor or the mid-depth of the cube (Fig. 12a). The result shows a negative self-potential anomaly of a few millivolts above the body in the ocean (Fig. 12c). The deeper part of a buried body is, as expected, associated with a positive self-potential (lower panel in Fig. 12c).

The second case corresponds to the horizontal geo-battery (Fig. 11b) considers a thin conductor of 200 m × 20 m in the horizontal directions and 10 m in the vertical direction placed beneath the seafloor, with the mid-depth being 30 m below the seafloor and the vertical redox boundary crossing the midpoint of the longest axis (Fig. 12b). The result shows a pair of positive and negative self-potential anomalies of a few millivolts above the

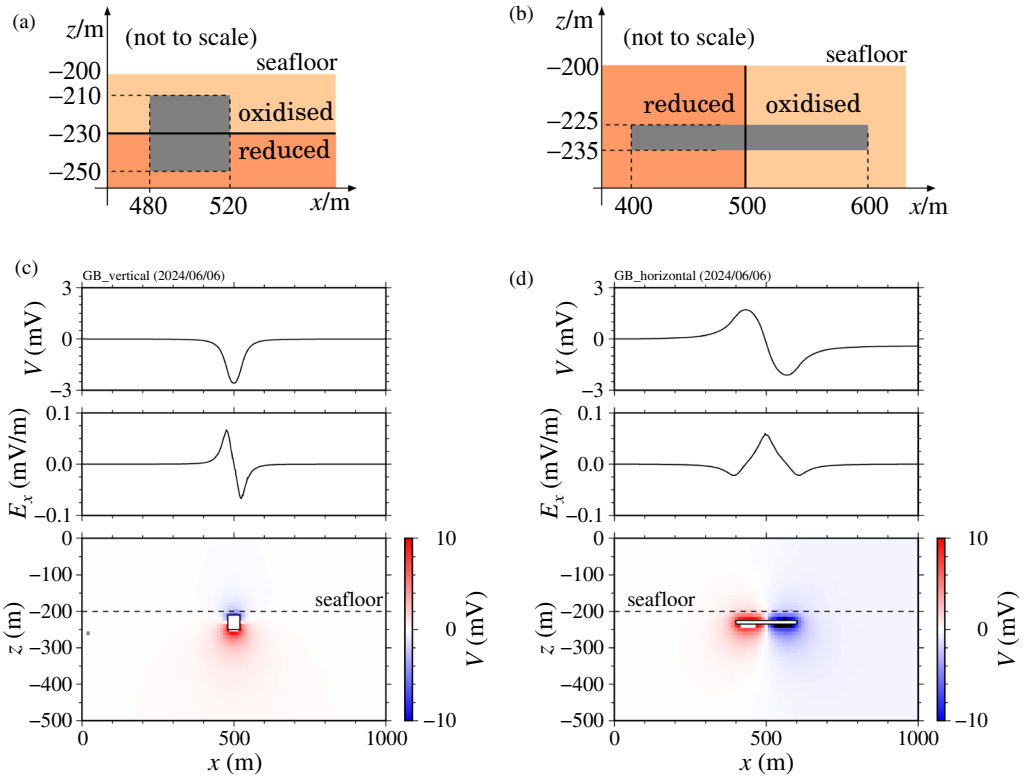

Fig. 12 Geometry and redox distribution used for the redox potential calculation and the results. **a**, **b** Geometry of a buried object (electrode) beneath the seafloor and the distribution of reduced and oxidised conditions, where anodic and cathodic reactions mainly occur respectively. **a** A cube (40 m in each direction) crosses the horizontal redox front corresponding to the vertical geo-battery of Sato and Mooney (1960) (Fig. 11a) and **b** a thin (10 m) and long (200 m) body crosses the vertical redox front corresponding to the horizontal geo-battery proposed in this study (Fig. 11b). The full boundary conditions are given in Additional file 2: Figure E1. **c**, **d** Results of (**a**, **b**) along the mid-plane. (Upper) Self-potential on the seafloor above the centre of the buried body. (Middle) Horizontal electric field on the seafloor above the centre of the buried body. (Lower) Cross-section of the self-potential over the centre of the buried body. The seafloor is indicated by the dashed line

body that can be observed in the seawater (Fig. 12d). The oxidised part causes a negative self-potential anomaly, as in the vertical geo-battery (lower panel in Fig. 12d), while the reduced part causes a positive anomaly near the seafloor. A long body (~200 m) is required to separate these anomalies with this spatial scale (e.g. Fig. 9a). A larger surface area leads to a more intense self-potential anomaly in both cases. Therefore, estimating the surface area involved in chemical reactions, which is a task for the resistivity survey, is critical to understanding the strength of the geo-battery.

The horizontal geo-battery model raises two issues relating to the present observation. The first issue is the origin of the disturbed redox horizon. In principle, the strong fluid flow of seawater could suppress the exposure of the low-Eh region, leading to the oxidised state in deeper parts and forming the negative self-potential anomaly. Since the estimated fluid flow near an active area with a negative self-potential anomaly (S9) (Fig. 10e) is more intense than that in a less-active area with a positive self-potential anomaly (S6) (Fig. 10d), this idea can be supported if the overall hydrothermal circulation, including the upwelling as a counterpart, behaves similarly (Fig. 11b). In a hydrothermal field called Suiyo Seamount located ~700 km south of the present study area, strong downward flows of small-scale convection have been suggested to occur around the main upwelling flow (e.g. Kinoshita et al. 2006). This partly supports our view. The second issue is whether the mechanism of exposing the reduced part of the geo-battery can produce a large (e.g. +100 mV) positive self-potential anomaly above the seafloor. For this mechanism to work, the reduced part, which is normally buried at depth, should be stable near the seafloor. If the mechanism is unable to produce such a large positive self-potential anomaly, the present result is achieved because the negative counterpart is weak. The absence of a large positive self-potential anomaly to date would seem to support this view.

6.2 Thermal and streaming potentials

Let us consider another possibility in which the effects of the thermal and streaming potentials contribute to the observed self-potential anomalies. This differs from the previous electrochemical model in terms of the distribution of a conductive body beneath the seafloor, and these two models would therefore be resolved by resistivity prospecting. We consider a situation where a 100-m-thick and 1000-m-wide layer of sediment is heated from below and overlain by a 200-m-thick layer of ocean.

We construct a two-dimensional conceptual model for the streaming and thermal potentials in the ocean in the presence of subseafloor hydrothermal circulation using *COMSOL multiphysics*. The model is divided into two submodels: (1) the heat and fluid transport submodel; and (2) the thermal/streaming potentials submodel. The thermal potential and the streaming potential are calculated independently to discuss these effects separately. The heat/fluid flow submodel is similar to our previous model (e.g. Kawada et al. 2011), while the streaming potential submodel is similar to that introduced in Ishido (1981). The thermal potential submodel is new but follows Ishido (1981). See Additional file 2: Appendix F for the details of the model and parameter values used in the model.

6.2.1 Heat and fluid transport

Two cases are considered. The first case assumes uniform basal heating but only the 300-m-wide part of the sediment layer is permeable for fluid flow (Fig. 13a). In this case, the flow in the permeable layer has two small-scale convection cells consisting of focused upwelling (the Darcy velocity is of the order of 10^{-8} m/s) surrounded by slow and wide downwelling (Fig. 13a). We refer to this flow structure as small-scale convection cells. The temperature in the permeable layer is high in the upwelling and low in the downwelling. The temperature field outside the permeable layer is in the thermal conduction state, where the temperature varies linearly with depth.

The second case assumes partial basal heating but the entire sediment layer is permeable. In this case, the flow forms a single-pass wide convection cell with focused upwelling at the high-temperature corner and diffuse downwelling outside the upwelling flow (Fig. 14a). We refer to this flow structure as a single-pass wide convection cell. The temperature structure around the upwelling plume is similar to the previous case. However, in contrast to the previous case, the temperature field of the downwelling region is maintained at seawater temperature, as there is no heat source there.

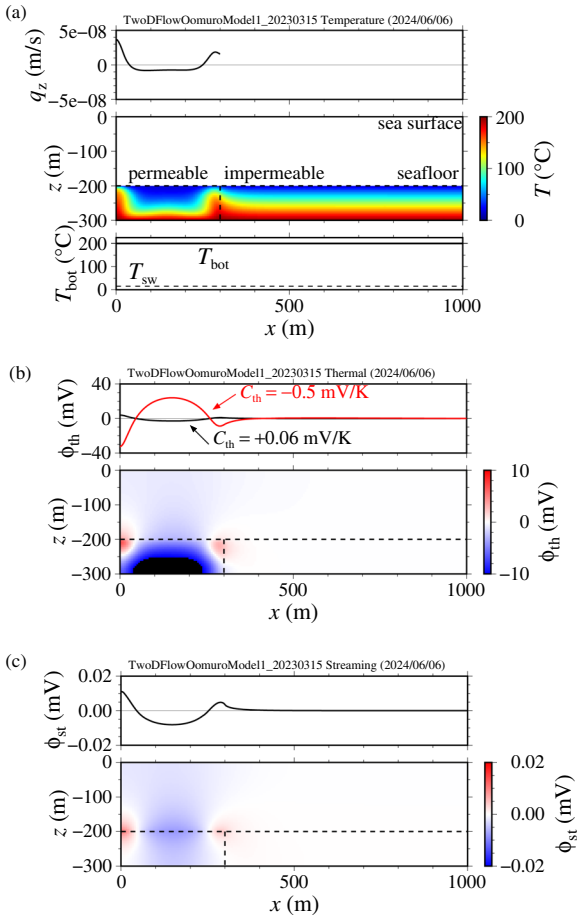

Fig. 13 Results of the thermal/streaming potentials model with small-scale convection cells. **a** Results of the heat and flow transport submodel. (Upper) Discharge/recharge Darcy velocity at the seafloor. (Middle) Temperature field below the seafloor with the colour scale shown on the right. (Lower) The temperatures at the top boundary (or the seafloor; T_{sw}) and the bottom boundary (T_{bot}) as the boundary conditions. **b** Results of the thermal potential submodel. (Upper) Self-potential along the seafloor. The black and red curves correspond to the coupling coefficients of +0.06 mV/K and −0.5 mV/K, respectively. (Lower panel) Self-potential in the ocean and the sediment with the coupling coefficients of +0.06 mV/K. The seafloor and the boundary between the permeable/impermeable areas are indicated by the dashed lines. **c** Results of the streaming potential submodel. The notation follows (**b**). The full boundary conditions can be found in Additional file 2: Figure F1

6.2.2 Thermal potential

The thermal potential is caused by differences in the mobility of ions at different temperatures. This effect is thought to contribute to self-potential anomalies up to the order of 100 millivolts above a high-temperature heat source such as a magma body (Corwin and Hoover 1979) or a coal fire (Revil et al. 2013) in on-land environments.

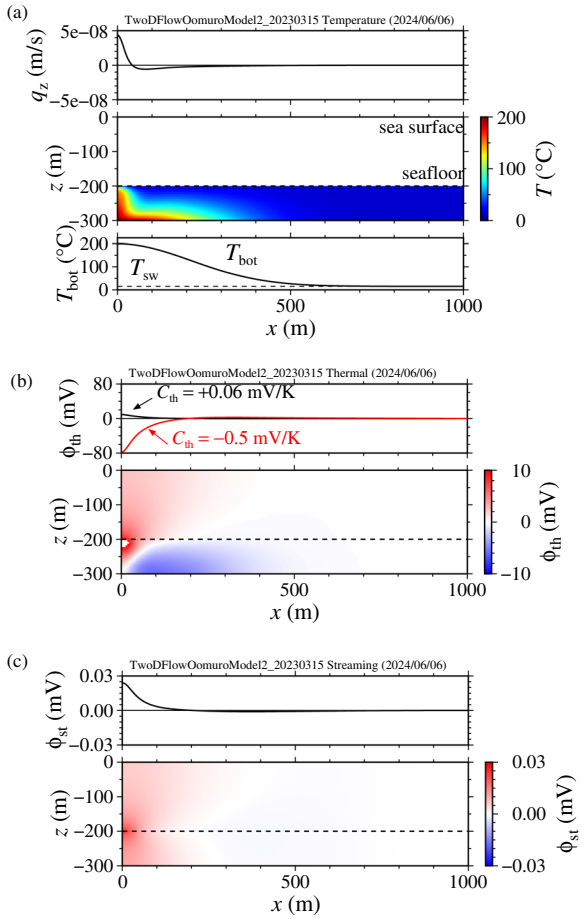

Fig. 14 Results of the thermal/streaming potentials model with a single-pass convection cell. **a** Results of the heat and flow transport submodel. **b** Results of the thermal potential submodel. **c** Results of the streaming potential submodel. The notation follows Fig. 13

However, the coupling coefficient $C_{th} = (\Delta\phi/\Delta T)$, defined as a proportional coefficient between the resulting electrostatic potential difference and the applied temperature difference, takes either positive or negative values between ±1 mV/K (e.g. Nourbehechet 1963; Fitterman and Corwin 1982; Leinov et al. 2010; Leinov and Jackson 2014; Revil et al. 2016). In general, clean surfaces that dominate the pore fluid conductivity tend to have positive values of C_{th}, while dirty surfaces that dominate the surface conductivity favour negative values (Revil et al. 2016). Increasing the pore salinity changes C_{th} from positive to negative at a certain salinity (Leinov and Jackson 2014; Revil et al. 2016), but the transition salinity and the degree of change depend on the conditions involved. Therefore, in the present study, we choose two typical values for the coupling coefficient, +0.06 mV/K and −0.5 mV/K.

Taking small-scale convection cells (Fig. 13a) with a small positive thermoelectric coupling coefficient, +0.06 mV/K, results in a positive self-potential anomaly above fluid discharges and a negative self-potential anomaly above fluid recharges with the amplitudes of ~5 mV (the black curve in the upper panel of Fig. 13b). The sources of the positive self-potential anomalies are concentrated in the upwelling plumes near the seafloor, around which the in situ self-potential takes a large value (the lower panel of Fig. 13b). The in situ self-potential takes the minimum value of less than −10 mV at depth. The positive and negative current sources are balanced in strength, and the self-potential away from the convecting area is almost zero. Switching a large negative thermoelectric coupling coefficient, −0.5 mV/K, reverses the above result. The self-potential anomaly now becomes negative above the fluid discharges and positive above the fluid recharges. The amplitude is ~40 mV (the red curve in the upper panel of Fig. 13b).

Taking a single-pass wide convection cell (Fig. 14a) with a small positive coupling coefficient (+0.06 mV/K) results in only the positive self-potential anomaly above the fluid discharge and a considerable part of the downwelling region (the black curve in the upper panel of Fig. 14b). The negative counterpart is not visible because the downwelling is diffuse in this case. The magnitude of the positive anomaly is larger than in the previous case, ~10 mV (the black curve in the upper panel of Fig. 14b). This increase is also due to the effect of the focused upwelling relative to the diffuse downwelling, compared to the previous case. Switching the coupling coefficient to −0.5 mV/K reverses the result, as in the previous case, and the negative self-potential anomaly arises. The self-potential reaches −80 mV (the red curve in the upper panel of Fig. 14b).

The above results suggest two possible scenarios to explain the observed paired self-potential anomalies in the Oomuro-dashi hydrothermal field by the thermal potential. The first scenario (Fig. 11c) does not require a conductive body below the seafloor, in which small-scale convection cells with a negative (but small) coupling coefficient are assumed. The recharge flow forms the positive self-potential, and the discharge flow forms the negative self-potential (the red curve in the upper panel of Fig. 13b, but the coupling coefficient should be smaller than in the present demonstration to match the observation). The second scenario (Fig. 11d) requires a conductive body only below the negative self-potential area, in which a large-scale single-pass fluid flow with a positive coupling coefficient is combined with the vertical geobattery. The fluid flow forms the positive self-potential above both the fluid discharge and recharge areas (the

black curve in the upper panel of Fig. 14b), while the vertical geo-battery forms the negative self-potential above the most intense fluid discharge areas.

The above calculations raise a serious issue for previous observations. A single-pass flow model with a large and negative coupling coefficient (the red curve in the upper panel of Fig. 14b) solely explains the previous observations with negative self-potential anomalies (e.g. Sato et al. 2017; Safipour et al. 2017; Kawada and Kasaya 2017, 2018; Constable et al. 2018; and many subsequent studies). The thermal potential, rather than the redox potential, seems to explain the results of all previous observations. However, one previous observation contradicts this view, in which the self-potential anomaly above a large ore body with less-active hydrothermal circulation was more intense than that above active hydrothermal vents discharging high-temperature fluids (Kawada and Kasaya 2017). Although the thermal potential may be able to contribute to some of the observed self-potential, a quantitative estimate cannot be made as we lack information on the coupling coefficient for marine hydrothermal deposits.

6.2.3 Streaming potential

The streaming potential is caused by the electrokinetic effect between the pore fluid and the surrounding sediments or rocks (e.g. Jouniaux and Ishido 2012; Revil and Jardani 2013). It emerges where fluid flow crosses discontinuities of the electrokinetic coefficient $C_{st} = (\Delta\phi/\Delta p_{ex})$, which is defined as a proportional coefficient between the resulting electrostatic potential and the applied (excess) fluid pressure (e.g. Ishido and Mizutani 1981; Jardani and Revil 2009). In a homogeneous geological structure, the seafloor is only the discontinuity for the coefficient, where C_{st} changes from a finite value (usually $C_{st} < 0$ below the seafloor, corresponding to a negative zeta potential) to zero (above the seafloor). We use this approximation following Ishido (1981) and choose a typical parameter value for the coupling coefficient corresponding to seawater salinity, -2×10^{-9} V/Pa (Glover et al. 2012).

The resulting self-potential patterns above the seafloor are similar to those considering the thermal potential with positive coupling coefficients (compare the black curves in the upper panels of Fig. 13b with 13c and those in Fig. 14b with c), although in this study the sources for the streaming potential are concentrated at the seafloor. In general, the resulting streaming potential in the ocean is positive above the upwellings and negative above the downwellings (Fig. 13c), similar to those observed in on-land environments (e.g. Ishido 1981; Jardani and Revil 2009). However, the magnitude of the streaming potential (~0.01 mV) is two orders of magnitude smaller than that of the thermal potential both for small-scale convection cells (Fig. 13a) and for a single-pass wide convection cell (Fig. 14a).

The streaming potential becomes a major contributor if the Darcy velocity could be much larger than the present demonstration (i.e., the downflow of $>10^{-7}$ m/s is expected from the temperature measurements; Fig. 10), and the coupling coefficient could be much larger than our conservative assumption (e.g. Glover et al. (2012)). If each contribution is an order of magnitude larger than the present estimate, the resulting self-potential of a few millivolts is comparable to the expected thermal potential anomaly with a small thermal coupling coefficient. With this assumption, a situation similar to Fig. 11c is unlikely to occur for small-scale convection cells with negative streaming coupling coefficients (e.g. Fig. 13a). A positive/negative self-potential is accompanied by a fluid discharge/recharge, which is controversial to the previous observations of negative self-potential anomalies above active areas, where the discharge flow tends to dominate. Positive coupling coefficients, although it is rare (e.g. Hase et al. 2003), may resolve this issue. A situation like Fig. 11d is plausible with a negative coupling coefficient when combined with the vertical geo-battery, in which an upward flow causes a positive self-potential anomaly over a hydrothermally active area due to large-scale convection (e.g. Fig. 14a), and the vertical geo-battery causes a negative potential anomaly. However, we cannot conclude that the streaming potential is the major contributor to the observed positive self-potential anomaly unless the electrokinetic coupling coefficient for hydrothermal precipitates is found to be negative and sufficiently large (for Fig. 11d), or positive (for Fig. 11c).

7 Conclusions

During two expeditions MR16-01 and KM16-03 in the Oomuro-dashi hydrothermal field, in the northern Izu-Ogasawara Arc, we observed a pair of negative and positive self-potential anomalies. This is the first detailed report of a positive self-potential anomaly around seafloor hydrothermal systems, although there have been a number of reports of negative self-potential anomalies. The negative self-potential anomaly coincides with the most intense part of the hydrothermal area, which is consistent with previous reports. In contrast, the positive anomaly is found in a relatively less-active area. This may differ from on-land environments, where negative and positive self-potential anomalies have been observed separately or simultaneously at a single site, but a pair of positive and negative self-potential anomalies with similar magnitudes are rare even on lands.

Based on the numerical modelling, we propose two new end-member models for the subsurface structure in

accordance with the paired self-potential anomaly. *The horizontal geo-battery model* assumes that the reduced part exposed near the seafloor is cut by a horizontally elongated conductive body (Fig. 11b). This model is partially supported by the temperature measurements and is more plausible at present. *The thermal/streaming potentials model* assumes that the pore-scale kinetic effects driven by the subsurface heat and fluid transports contribute to the self-potential anomalies and do not require conductive bodies (Fig. 11c). In addition, a combined situation can occur, where both the thermal/streaming potentials and the vertical geo-battery contribute to the paired anomaly (Fig. 11d). These models can be distinguished by the presence or absence of buried conductive bodies after obtaining information on the subsurface geological/electrical structures. Systematic surveys above the observed paired self-potential anomalies may provide new insights into the fluid flow and chemical reactions in hydrothermal systems. Mapping the electrical conductivity of the subseafloor using resistivity surveys may more accurately constrain the source locations to distinguish (or reject) the models proposed above. In addition, deep-sea drilling may provide a better understanding of the structure of the deep subseafloor.

Abbreviations

AM	Amur Plate
CTD	Conductivity-temperature-depth
FEM	Finite element method
FRP	Fibre-reinforced plastics
GMT	Generic mapping tools
JAMSTEC	The Japanese Agency for Marine-Earth Science and Technology
MBES	Multi-beam echo sounder
MTL	Miniaturised temperature data logger
OK	Okhotsk Plate
PA	Pacific Plate
PS	Philippine Sea Plate
RMS	Root mean square
SAHF	Stand-alone heat-flow meter
SSBL	Super-short baseline

Supplementary Information

The online version contains supplementary material available at https://doi.org/10.1186/s40623-024-02056-x.

Additional file 1: Fig. S1: Photographs of the hydrothermal area taken during expedition NT15-21. Fig. S2: Cable angles along the survey tracks. Fig. S3: Cross-sectional view of the results obtained during the expedition KM16-03 including Ch.1. Fig. S4: Time series of all temperature sensors. Fig. S5: Results of the time-series analysis, complementary to Figs. 8 and 10. Fig. S6: RMS misfit between the shallow and deep temperature time series for each sensor combination. Fig. S7: Misfit between the observed and reconstructed temperature time series.

Additional file 2: Appendix A: Simplified source inversion for the self-potential data. Appendix B: Forward self-potential calculation to verify the inverted potential. Appendix C: Estimation of fluid velocity from a long-term temperature record. Appendix D: Estimation of Darcy velocity from a curved temperature profile. Appendix E: Redox potential calculation using a simplified geo-battery model. Appendix F: Subsurface fluid flow model for the calculation of thermal/streaming potentials.

Acknowledgements
This study was supported by the Cross-ministerial Strategic Innovation Promotion Program "Next-generation Technology for Ocean Resources Exploration" launched by the Council for Science, Technology and Innovation (CSTI) and managed by the Japan Agency for Marine-Earth Science and Technology (JAMSTEC). We thank the captains and crews of R/V Mirai (MR16-01), R/V Kaimei (KM16-03), R/V Natsushima (NT15-21), R/V Shinsei-maru (KS-16-J01), the chief scientists T. Hyakudome (MR16-01) and M. Torigoe (KM16-03), and T. Yokobiki (NT14-E02, NT15-21, and KS-16-J06), and the on-board scientists (especially for T. Ohki in the selection of photographs displayed in Fig. 2 and Additional file 1: Figure S1a) and marine technicians for their observational support during the expeditions. The bathymetric map was compiled from the SSBL data of the expedition NT14-E02 by T. Kodera. Most of the figures were drawn using the Generic Mapping Tools software version 6 (Wessel et al., 2019). Comments from two anonymous reviewers and the handling editor are valuable in improving the quality of the manuscript.

Author contributions
TK designed the instrument, conducted the observations, and performed the initial data analysis. YK conducted the main data analysis, developed numerical models, performed numerical calculations, and prepared the manuscript, figures, and tables. YK and TK discussed the results and approved the final version of the manuscript.

Funding
Expeditions MR16-01 and KM16-03 were supported by the *Cross-ministerial Strategic Innovation Promotion Program "Next-generation Technology for Ocean Resources Exploration"* launched by the *Council for Science, Technology and Innovation* (CSTI).

Availability of data and materials
The datasets used and/or analysed during the current study are available from the corresponding author upon reasonable request.

Declarations

Ethics approval and consent to participate
Not applicable.

Consent for publication
Not applicable.

Competing interests
The author declares that they have no competing interests.

Author details
[1]Japan Agency for Marine-Earth Science and Technology, 2-15 Natsushima-Cho, Yokosuka 237-0061, Japan. [2]Graduate School of Science, The University of Tokyo, 7-3-1 Hongo, Bunkyo-Ku, Tokyo 113-0033, Japan.

Received: 28 March 2024 Accepted: 8 August 2024
Published online: 26 September 2024

References

Bigalke J, Grabner EW (1997) The geobattery model: a contribution to large scale electrochemistry. Electrochim Acta 42(23–24):3443. https://doi.org/10.1016/S0013-4686(97)00053-4

Bird P (2003) An updated digital model of plate boundaries. Geochem Geophys Geosyst 4(3):1027. https://doi.org/10.1029/2001GC000252

Bischoff JL, Rosenbauer RJ (1988) Liquid-vapor relations in the critical region of the system NaCl–H_2O from 380 to 415 °C: a refined determination of the critical point and two-phase boundary of seawater. Geochim Cosmochim Acta 52(8):2121. https://doi.org/10.1016/0016-7037(88)90192-5

Bredehoeft JD, Papadopulos IS (1965) Rates of vertical groundwater movement estimated from the Earth's thermal profile. Water Resour Res 1(2):325. https://doi.org/10.1029/WR001i002p00325

Castermant J, Mendonça CA, Revil A, Trolard F, Bourrié G, Linde N (2008) Redox potential distribution inferred from self-potential measurements associated with the corrosion of a burden metallic body. Geophys Prospect 56(2):269. https://doi.org/10.1111/j.1365-2478.2007.00675.x

COMSOL Inc. (2016) Galvanized Nail. https://www.comsol.jp/model/galvanized-nail-14015 Accessed 27 Mar 2023

Constable S, Kowalczyk P, Bloomer S (2018) Measuring marine self-potential using an autonomous underwater vehicle. Geophys J Int 215(1):49. https://doi.org/10.1093/gji/ggy263

Corwin RF, Hoover DB (1979) The self-potential method in geothermal exploration. Geophysics 44(2):226. https://doi.org/10.1190/1.1440964

Evans RL (1996) A seafloor gravity profile across the TAG hydrothermal mound. Geophys Res Lett 23(23):3447–3450. https://doi.org/10.1029/96GL00734

Filloux JH (1987) Instrumentation and experimental methods for oceanic studies. In: Jacobs JA (ed) Geomagnetism, vol 1. Academic Press, Cambridge, p 143

Fitterman DV, Corwin RF (1982) Inversion of self-potential data from the Cerro Prieto geothermal field, Mexico. Geophysics 47(6):938. https://doi.org/10.1190/1.1441361

Glover PWJ, Walker E, Jackson MD (2012) Streaming-potential coefficient of reservoir rock: a theoretical model. Geophysics 77:D17. https://doi.org/10.1190/geo2011-0364.1

Goto S, Yamano M, Kinoshita M (2005) Thermal response of sediment with vertical fluid flow to periodic temperature variation at the surface. J Geophys Res 110:B01106. https://doi.org/10.1029/2004JB003419

Hamamoto H, Yamano M, Goto S (2005) Heat flow measurement in shallow seas through long-term temperature monitoring. Geophys Res Lett 32(21):L21311. https://doi.org/10.1029/2005GL024138

Hamuro K, Aramaki S, Fujioka K, Ishii T, Tanaka T, Uto K (1983) The Higashi-Izu-oki Submarine volcanoes, part 2, and the submarine volcanoes near the Izu Shoto islands. Bull Earthquake Res Inst 58(2):527. https://doi.org/10.15083/0000032961 (**in Japanese with English abstract and figure captions**)

Hansen PC (2001) The L-curve and its use in the numerical treatment of inverse problems. In: Hansen PC, Johnston P (eds) Computational inverse problems in electrocardiology. WIT Press, Southampton

Hase H, Ishido T, Takakura S, Hashimoto T, Sato K, Tanaka Y (2003) ζ potential measurement of volcanic rocks from Aso caldera. Geophys Res Lett 30(23):2210. https://doi.org/10.1029/2003GL018694

Heinson G, White A, Constable S, Key K (1999) Marine self potential exploration. Explor Geophys 30:1. https://doi.org/10.1071/EG999001

Heinson G, White A, Robinson D, Fathianpour N (2005) Marine self-potential gradient exploration of the continental margin. Geophysics 70:G109. https://doi.org/10.1190/1.2057981

Honsho C, Ura T, Kim K, Asada A (2016a) Postcaldera volcanism and hydrothermal activity revealed by autonomous underwater vehicle surveys in Myojin Knoll caldera, Izu-Ogasawara. Arc J Geophys Res 121:4085. https://doi.org/10.1002/2016JB012971

Honsho C, Yamazaki T, Ura T, Okino K, Morozumi H, Ueda S (2016b) Magnetic anomalies associated with abundant production of pyrrhotite in a sulfide deposit in the Okinawa Trough, Japan. Geochem Geophys Geosyst 17:4413. https://doi.org/10.1002/2016GC006480

Ishibashi JI, Noguchi T, Toki T, Miyabe S, Yamagami S, Onishi Y, Yamanaka T, Yokoyama Y, Omori E, Takahashi Y, Hatada K, Nakaguchi Y, Yoshizaki M, Konno U, Shibuya T, Takai K, Inagaki F, Kawagucci S (2014) Diversity of fluid geochemistry affected by processes during fluid upwelling in active hydrothermal fields in the Izena Hole, the middle Okinawa Trough back-arc basin. Geochem J 48:357. https://doi.org/10.2343/geochemj.2.0311

Ishibashi JI, Okino K, Sunamura M (2015) Subseafloor biosphere linked to hydrothermal systems: TAIGA concept. Springer, Tokyo. https://doi.org/10.1007/978-4-431-54865-2

Ishido T (1981) Streaming potential associated with hydrothermal convection in the crust a possible mechanism of self-potential anomalies in geothermal areas. J Geotherm Res Soc Jpn 3(2):87. https://doi.org/10.11367/grsj1979.3.87. (**in Japanese with English abstract and figure captions**)

Ishido T, Mizutani H (1981) Experimental and theoretical basis of electrokinetic phenomena in rock-water systems and its applications to geophysics. J Geophys Res 86(B3):1763. https://doi.org/10.1029/JB086iB03p01763

Ishido T, Pritchett JW, Tosha T, Nishi Y, Nakanishi S (2013) Monitoring underground migration of sequestered CO_2 using self-potential methods. Energy Proc 37:4077. https://doi.org/10.1016/j.egypro.2013.06.308

JAMSTEC (2012) First discovery of submarine volcanic activity at Omurodashi, south of Izu-Oshima. https://www.jamstec.go.jp/e/about/press_release/20121011/ Accessed 9 Dec 2022

Jardani A, Revil A (2009) Stochastic joint inversion of temperature and self-potential data. Geophys J Int 179:640. https://doi.org/10.1111/j.1365-246X.2009.04295.x

Jouniaux L, Ishido T (2012) Electrokinetics in earth sciences: a tutorial. Int J Geophys 2012:286107. https://doi.org/10.1155/2012/286107

Kawada Y, Kasaya T (2017) Marine self-potential survey for exploring seafloor hydrothermal ore deposits. Sci Rept 7:13552. https://doi.org/10.1038/s41598-017-13920-0

Kawada Y, Kasaya T (2018) Self-potential mapping using an autonomous underwater vehicle for the sunrise deposit, Izu-Ogasawara arc, southern Japan. Earth Planet Space 70:142. https://doi.org/10.1186/s40623-018-0913-6

Kawada Y, Seama N, Urabe T (2011) The role of seamounts in the transport of heat and fluids: relations among seamount size, circulation patterns, and crustal heat flow. Earth Planet Sci Lett 306(1–2):55. https://doi.org/10.1016/j.epsl.2011.03.029

Kasaya T, Goto TN, Iwamoto H, Kawada Y (2019) Development of multi-purpose electromagnetic survey instruments. In: The 13th SEGJ International Symposium, p 159. https://doi.org/10.1190/SEGJ2018-042.1

Kawagucci S, Chiba H, Ishibashi JI, Yamanaka T, Toki T, Muramatsu Y, Ueno Y, Makabe A, Inoue K, Yoshida N, Nakagawa S, Nunoura T, Takai K, Takahata N, Sano Y, Narita T, Teranishi G, Obata H, Gamo T (2011) Hydrothermal fluid geochemistry at the Iheya North field in the mid-Okinawa trough: implication for origin of methane in subseafloor fluid circulation systems. Geochem J 45(2):109. https://doi.org/10.2343/geochemj.1.0105

Kinoshita M, Kawada Y, Tanaka A, Urabe T (2006) Recharge/discharge interface of a secondary hydrothermal circulation in the Suiyo Seamount of the Izu-Bonin arc, identified by submersible-operated heat flow measurements. Earth Planet Sci Lett 245:498. https://doi.org/10.1016/j.epsl.2006.02.006

Leinov E, Vinogradov J, Jackson MD (2010) Salinity dependence of the thermoelectric coupling coefficient in brine-saturated sandstones. Geophys Res Lett 37:L23308. https://doi.org/10.1029/2010GL045379

Leinov E, Jackson MD (2014) Experimental measurements of the SP response to concentration and temperature gradients in sandstones with application to subsurface geophysical monitoring. J Geophys Res 119(B9):6855. https://doi.org/10.1002/2014JB011249

Masaki Y, Kinoshita M, Inagaki F, Nakagawa S, Takai K (2011) Possible kilometer-scale hydrothermal circulation within the Iheya-North field, mid-Okinawa Trough, as inferred from heat flow data. JAMSTEC Rept Res Dev 12:1. https://doi.org/10.5918/jamstecr.12.1

McBirney AR (1963) Factors governing the nature of submarine volcanism. Bull Volcanol 26(1):455. https://doi.org/10.1007/BF02597304

McIntosh IM, Tani K, Nichols AR, Chang Q, Kimura JI (2022) Past eruptions of a newly discovered active, shallow, silicic submarine volcano near Tokyo Bay, Japan. Geology 50(10):1111. https://doi.org/10.1130/G50148.1

Mehanee S (2015) Tracing of paleo-shear zones using self-potential data inversion: case studies from the KTB, Rittsteig, and Grossensees graphite-bearing fault planes. Earth Planet Space 67:14. https://doi.org/10.1186/s40623-014-0174-y

Mehanee S, Essa KS, Soliman K, Diab ZE (2023) A fast imaging method for the interpretation of self-potential data with application to geothermal systems and mineral exploration. Sci Rept 3:13548. https://doi.org/10.1038/s41598-023-39672-8

METI (2013) Report for the first stage of the program. Development of Deep-sea Mineral Resources. http://www.meti.go.jp/press/2013/07/20130705003/20130705003-2.pdf Accessed 9 Dec 2022 (**in Japanese**)

Minsley BJ, Sogade J, Morgan FD (2007) Three-dimensional source inversion of self-potential data. J Geophys Res 112:B02202. https://doi.org/10.1029/2006JB004262

Mizuno K, White WB (1983) Annual and interannual variability in the Kuroshio current system. J Phys Oceanogr 13:1847. https://doi.org/10.1175/1520-0485(1983)013%3c1847:AAIVIT%3e2.0.CO;2

Naudet V, Revil A, Rizzo E, Bottero JY, Bégassat P (2004) Groundwater redox conditions and conductivity in a contaminant plume from geoelectrical investigations. Hydrol Earth Syst Sci 8(1):8–22. https://doi.org/10.5194/hess-8-8-2004

Nourbehechet B (1963) Irreversible thermodynamic effects in inhomogeneous media and their applications in certain geoelectric problems. Dissertation, Massachusetts Institute of Technology. https://dspace.mit.edu/handle/1721.1/11576 Accessed 9 Dec 2022

Ohki T, Yokobiki T, Nishida S, Kasaya T, Kodera T, Toizumi M, Tani K, Kawaguchi K (2018) Survey method and sea trials for construction of cable-based observation system on seafloor with hydrothermal activity. JAMSTEC Rept Res Dev 26:21. https://doi.org/10.5918/jamstecr.26.21. (**in Japanese with English abstract and figure captions**)

Ohmoto H (1996) Formation of volcanogenic massive sulfide deposits: the Kuroko perspective. Ore Geol Rev 10(3–6):135. https://doi.org/10.1016/0169-1368(95)00021-6

Pfender M, Villinger H (2002) Miniaturized data loggers for deep sea sediment temperature gradient measurements. Mar Geol 186:557. https://doi.org/10.1016/S0025-3227(02)00213-X

Revil A, Jardani A (2013) The self-potential method: theory and applications in environmental geosciences. Cambridge University Press, Cambridge. https://doi.org/10.1017/CBO9781139094252

Revil A, Karaoulis M, Srivastava S, Byrdina S (2013) Thermoelectric self-potential and resistivity data localize the burning front of underground coal fires. Geophysics 78(5):B259. https://doi.org/10.1190/geo2013-0013.1

Revil A, Meyer CD, Niu Q (2016) A laboratory investigation of the thermoelectric effect. Geophysics 81(4):E243. https://doi.org/10.1190/geo2015-0281.1

Revil A, Finizola A, Gresse M (2023) Self-potential as a tool to assess groundwater flow in hydrothermal systems: a review. J Volcanol Geotherm Res 437:107788. https://doi.org/10.1016/j.jvolgeores.2023.107788

Safipour R, Hölz S, Halbach J, Jegen M, Petersen S, Swidinsky A (2017) A self-potential investigation of submarine massive sulfides: Palinuro Seamount, Tyrrhenian Sea. Geophysics 82:A51. https://doi.org/10.1190/geo2017-0237.1

Sato S, Goto T, Kasaya T, Kawada Y, Iwamoto H, Kitada K (2017) Noise reduction method of marine spontaneous electric field data using independent component analysis. Butsuri-Tansa 70:42. https://doi.org/10.3124/segj.70.42. (**in Japanese with English abstract and figure captions**)

Sato M, Mooney HM (1960) The electrochemical mechanism of sulfide self-potentials. Geophysics 25:226. https://doi.org/10.1190/1.1438689

Su Z, Tao C, Zhu Z, Revil A, Shen J, Nie Z, Li Q, Deng X, Zhou J, Liu L (2022) Joint interpretation of marine self-potential and transient electromagnetic survey for seafloor massive sulfide (SMS) deposits: application at TAG hydrothermal mound, Mid-Atlantic Ridge. J Geophys Res 127:e2022JB024496. https://doi.org/10.1029/2022JB024496

Sugiyama M (2013) Machine learning illustrated. Kodansha Scientific, Tokyo (**in Japanese**)

Tamura Y, Tatsumi Y (2002) Remelting of an andesitic crust as a possible origin for rhyolitic magma in oceanic arcs: an example from the Izu-Bonin arc. J Petrol 43(6):1029. https://doi.org/10.1093/petrology/43.6.1029

Tamura Y, Gill JB, Tollstrup D, Kawabata H, Shukuno H, Chang Q, Miyazaki T, Takahashi T, Hirahara Y, Kodaira S, Ishizuka O, Suzuki T, Kido Y, Fiske RS, Tatsumi Y (2009) Silicic magmas in the Izu-Bonin oceanic arc and implications for crustal evolution. J Petrol 50(4):685. https://doi.org/10.1093/petrology/egp017

Tani K, Shukuno H, Hirahara Y, Masaki Y, Nichols A, Ishitsuka O, Fiske R, Cashman K, Leat P, Carey R, McIntosh I, Onoue A (2012) Oomurodashi Volcano: Preliminary results of the NT12–19 cruise. In: Programme and Abstracts, the Volcanological Society of Japan, p 145. https://doi.org/10.18940/vsj.2012.0_145 (**in Japanese**)

Tsuji T, Takai K, Oiwane H, Nakamura Y, Masaki Y, Kumagai H, Kinoshita M, Yamamoto F, Okano T, Kuramoto S (2012) Hydrothermal fluid flow system around the Iheya North Knoll in the mid-Okinawa trough based on seismic reflection data. J Volcanol Geotherm Res 213–214:41. https://doi.org/10.1016/j.jvolgeores.2011.11.007

Tsuru T, Okuda A, No T, Kaneda Y, Tamaki K (2008) Subsurface structure of the Myojin Knoll pumiceous volcano obtained from multichannel seismic reflection data. Earth Planet Space 60(7):721. https://doi.org/10.1186/BF03352820

Urabe T, Maruyama A, Marumo K, Seama N, Ishibashi JI (2005) The Archean Park project: interaction between microbiological and geological processes in deep-sea hydrothermal vent and sub-vent environments. Oceanogr Jpn 14(2):129. https://doi.org/10.5928/kaiyou.14.129. (**in Japanese with English abstract and figure captions**)

Wessel P, Luis JF, Uieda L, Scharroo R, Wobbe F, Smith WHF, Tian D (2019) The generic mapping tools version 6. Geochem Geophys Geosyst 20(11):5556. https://doi.org/10.1029/2019GC008515

Yoshizumi R, Miyoshi Y, Ishibashi JI (2015) The characteristics of the seafloor massive sulfide deposits at the Hakurei Site in the Izena Hole, the Middle Okinawa Trough. In: Ishibashi JI, Okino K, Sunamura M (eds) Subseafloor biosphere linked to hydrothermal systems. Springer, Tokyo, p 561. https://doi.org/10.1007/978-4-431-54865-2_43

Zhu Z, Tao C, Shen J, Revil A, Deng X, Liao S, Zhou J, Wang W, Nie Z, Yu J (2020) Self-potential tomography of a deep-sea polymetallic sulfide deposit on Southwest Indian Ridge. J Geophys Res 125:e2020JB019738. https://doi.org/10.1029/2020JB019738

Zlotnicki J, Nishida Y (2003) Review on morphological insights of self-potential anomalies on volcanoes. Surv Geophy 24(4):291–338. https://doi.org/10.1023/B:GEOP.0000004188.67923.ac

Publisher's Note